

# Possible Solution of the long-standing discrepancy in the Microlensing Optical Depth Toward the Galactic Bulge by correcting the stellar number count

T. Sumi<sup>1</sup>, M. T. Penny<sup>2,3</sup>

## ABSTRACT

We find that significant incompleteness in stellar number counts results in a significant overestimate of the microlensing optical depth  $\tau$  and event rate per star per year  $\Gamma$  toward the Galactic bulge from the first two years of the MOA-II survey. We find that the completeness in Red Clump Giant (RCG) counts  $f_{\text{RC}}$  decreases proportional to the galactic latitude  $b$ , as  $f_{\text{RC}} = (0.63 \pm 0.11) - (0.052 \pm 0.028) \times b$ , ranging between 1 and 0.7 at  $b = -6^\circ \sim -1.5^\circ$ . The previous measurements using all sources by Difference Image Analysis (DIA) by MACHO and MOA-I suffer the same bias. On the other hand, the measurements using a RCG sample by OGLE-II, MACHO and EROS were free from this bias because they selected only the events associated with the resolved stars. Thus, the incompleteness both in the number of events and stellar number count cancel out. We estimate  $\tau$  and  $\Gamma$  by correcting this incompleteness. In the central fields with  $|l| < 5^\circ$ , we find  $\Gamma = [18.74 \pm 0.91] \times 10^{-6} \exp[(0.53 \pm 0.05)(3 - |b|)] \text{ star}^{-1} \text{ yr}^{-1}$  and  $\tau_{200} = [1.84 \pm 0.14] \times 10^{-6} \exp[(0.44 \pm 0.07)(3 - |b|)]$  for the 427 events with  $t_E \leq 200$  days using all sources brighter than  $I_s \leq 20$  mag. Our revised all-source  $\tau$  measurements are about  $2\text{-}\sigma$  smaller than the other all-source measurements and are consistent with the RCG measurements within  $1\text{-}\sigma$ . We conclude that the long-standing problem on discrepancy between the high  $\tau$  with all-source samples by DIA and low  $\tau$  with RCG samples can probably be explained by the incompleteness of the stellar number count. A model fit to these measurements predicts  $\Gamma = 4.60 \pm 0.25 \times 10^{-5} \text{ star}^{-1} \text{ yr}^{-1}$  at  $|b| \sim -1^\circ.4$  and  $-2^\circ.25 < l < 3^\circ.75$  for sources with  $I < 20$ , where the future space mission WFIRST will observe.

*Subject headings:* gravitational lensing – Galaxy: bulge – stars: variables: other

---

<sup>1</sup>Department of Earth and Space Science, Graduate School of Science, Osaka University, Toyonaka, Osaka 560-0043, Japan,  
e-mail: sumi@ess.sci.osaka-u.ac.jp

<sup>2</sup>Department of Astronomy, Ohio State University, 140 W. 18th Ave., Columbus, OH 43210, USA

<sup>3</sup>Sagan Fellow

## 1. Introduction

The gravitational microlensing optical depth and the event rate toward the Galactic Bulge (GB) are known to be useful observables for the study of the stellar mass function and the structure and kinematics of the Galaxy, as these quantities, in addition to the microlensing timescale distribution are related to the masses and velocities of lens objects (Paczynski 1991, Griest et al. 1991, Novati et al. 2008). Currently, the microlensing survey groups: MOA-II<sup>1</sup>, OGLE-IV<sup>2</sup>, WiSE<sup>3</sup> (Shvartzvald & Maoz 2012) and KMTNet (Kim et al. 2010) are detecting a couple of thousand of microlensing events every year toward the GB.

The magnification of a microlensing event is described by the minimum impact parameter ( $u_0$ ) in units of Einstein radius  $R_E(M, D_s, D_l)$ , the time of maximum magnification ( $t_0$ ), the Einstein radius crossing time (or timescale) ( $t_E = R_E/v_t$ ), where  $v_t$  is the transverse velocity of the lens relative to the line of sight,  $M$  is the lens mass,  $D_s$  and  $D_l$  are the distance to the source and the lens, respectively (Paczynski 1986).

The microlensing optical depth,  $\tau$  is the probability that any given source star is magnified by more than 1.34 (corresponding to the source being inside the Einstein ring disk of the lens) at any given time. This is directly related to the mass density of compact objects along the line of sight (Paczynski 1996). Theoretically, it is simpler than the microlensing event rate, because it doesn't depend on the lens mass and lens-source relative velocity distribution.  $\tau$  can be determined observationally from the following expression,

$$\tau = \frac{\pi}{2N_s T_o} \sum_i \frac{t_{E,i}}{\varepsilon(t_{E,i})}. \quad (1)$$

where  $N_s$  is the total number of source stars monitored for microlensing,  $T_o$  is the duration of the survey in days,  $t_{E,i}$  is the Einstein radius crossing time for the  $i$ -th event, and  $\varepsilon(t_{E,i})$  is the detection efficiency at that time-scale. Because long  $t_E$  events give a large contribution to  $\tau$ , we present the observed optical depth with a subscript, which indicates the maximum  $t_E$  value allowed by each analysis.

The previous Galactic bulge microlensing optical depth results have been somewhat controversial (see details in Sumi et al. 2013). The first measurements of the optical depth,  $\tau_{100} \sim 3.3 \times 10^{-6}$  by OGLE (Udalski et al. 1994) and  $\tau_{150} \sim 3.9^{+1.8}_{-1.2} \times 10^{-6}$  by MACHO (Alcock et al. 1997), were well above the predictions of  $\tau \sim 5 \times 10^{-7}$  (Paczynski 1991;

---

<sup>1</sup><http://www.massey.ac.nz/~iabond/alert/alert.html>

<sup>2</sup><http://www.astrouw.edu.pl/~ogle/ogle4/ews/ews.html>

<sup>3</sup><http://wise-obs.tau.ac.il/~wingspan/>

Griest et al. 1991) and  $\tau \sim 8.5 \times 10^{-7}$  (Kiraga & Paczyński 1994). The later studies based on Difference Image Analysis (DIA), which is less sensitive to the systematics of blending in crowded fields, also found relatively high values of  $\tau_{150} \sim 2.5 \times 10^{-6}$  (at  $b \sim -3.5$ ) by MACHO (Alcock et al. 2000) and MOA (Sumi et al. 2003).

To explain high optical depths, the presence of a bar oriented along our line of sight to the GB have been suggested (Paczynski et al. 1994; Zhao, Spergel & Rich 1995; Han & Gould 2003; Zhao & Mao 1996; Peale 1998; Gyuk 1999). But their predictions range over  $\tau = 0.8 - 2.0 \times 10^{-6}$  and had difficulty explaining the observed high optical depths.

Alcock et al. (1997) raised the possibility of a systematic bias in the optical depth measurement due to the degeneracy between  $t_E$  and  $u_0$  in relatively low signal-to-noise ratio (S/N) events when the source base-line flux is unknown due to blending (c.f. Woźniak & Paczyński 1997; Han 1999; Bond et al. 2001; Gould & An 2002).

Popowski et al. (2001) proposed that optical depth may be estimated without any bias due to blending by using only events with bright source stars, such as Red Clump Giants (RCG), in which the blending might be negligible, rather than using all sources including the faint sources as in previous studies. Except for one high value measured by Alcock et al. (1997), the other measurements based on events with bright sources resulted in lower optical depths when measured by EROS (Afonso et al. 2003), MACHO (Popowski et al. 2005), and EROS (Hamadache et al. 2006).

However, Popowski et al. (2005) and Hamadache et al. (2006) realized that lensing of a fainter star that is unresolved from the bright star are common. But they also noted that this would increase the apparent number of bright star events, while it also make  $t_E$  shorter and these two effects would nearly cancel, so that it does not cause large bias in the optical depth. Sumi et al. (2006) and Smith, Woźniak, Mao & Sumi (2007) confirmed this cancelation by image level simulations. They also measured the bulge optical depth from OGLE-II for RCG sources with high S/N light curves, which allowed them to determine the source brightness and exclude events with faint sources. Thus, they do not rely on the lucky cancelation of the biases. Their result was consistent with the MACHO and EROS values. These values are consistent with predictions based on the revised COBE bar model by Han & Gould (1995), which has a mass of  $M_{\text{bulge}} = 1.62 \times 10^{10} M_{\odot}$  and the viewing angle  $\phi \sim 20^\circ$ , and the latest COBE elongated bar model by Bissantz & Gerhard (2002) with  $\phi \sim 20^\circ$ .

Although the optical depth difference between the RCG sources and the all sources by DIA are not very significant due their large errors, the DIA optical depth values are systematically larger than the RCG values. The reason for this is not well understood.

Sumi et al. (2013) made optical depth measurements using samples of 83 RCG events

and 474 all source events with well measured parameters from the DIA analysis of MOA-II data. This is the largest sample ever used for an optical depth measurement. Their optical depth measurement for all sources was in-between those of previous measurements, i.e., lower than all source samples and higher than RCG samples and concluded that previous discrepancy between all source sample and RCG sample were just a statistical fluctuation.

Sumi et al. (2013) pointed a possible problem on using the same luminosity function in all fields as the one in Baade’s window for estimating the number of sources at small level. But they did not consider the completeness of stellar number counts used to normalize that luminosity function. A systematic bias in the number counts of source stars will affect the measured optical depth. We investigate this point in this paper.

The event rate per star per year  $\Gamma$  is also affected by the same bias. This is important for the future space-based microlensing surveys (Bennett & Rhie 2002), like the exoplanet microlensing survey planned for WFIRST (Green et al. 2012; Spergel et al. 2015) or Euclid (Penny et al. 2013)

In this paper we estimate the completeness of the number count of the source stars and revise the measurement of the microlensing event rate and optical depth toward the GB based on the first two years of the MOA-II survey. We present the stellar number count in section § 2 and its completeness in section § 3. We present the revised event rate and optical depth results in section § 4. In section § 5 and § 6, we model the distribution of the optical depth and event rate with galactic coordinates. The discussion and conclusions are given in section § 7,

## 2. Stellar number count.

### 2.1. MOA Stellar number count

We use the same dataset as Sumi et al. (2013) which used the data taken in the 2006 and 2007 seasons by the MOA-II survey, with the 1.8-m MOA-II telescope located at the Mt. John University Observatory, New Zealand. The telescope is equipped with the mosaic CCD camera, MOA-cam3 (Sako et al. 2008), which has a  $2.18 \text{ deg}^2$  field of view (FOV) with a pixel scale of  $0.58 \text{ arcsec/pixel}$ . The median seeing for this dataset was  $\sim 2.0''$ .

The centers of the 22 GB fields of the MOA-II survey are listed in Table 1. The images were taken using the custom MOA-Red wide-band filter, which is equivalent to the sum of the standard Kron/Cousins  $R$  and  $I$ -bands. The average instrumental magnitudes of the MOA reference images were roughly calibrated to the Kron/Cousins  $I$ -band using OGLE-II

photometry map of the Galactic bulge (Udalski et al. 2002) within  $\sim 0.2$  mag.  $V$ -band images were taken occasionally in order to make instrumental color-magnitude diagrams (CMD).

The images were reduced with MOA’s implementation (Bond et al. 2001) of the difference image analysis (DIA) method (Tomany & Crotts 1996; Alard & Lupton 1998; Alard 2000). In the DIA method, a high-quality, good-seeing reference image is subtracted from each observed image after matching the seeing and photometric scaling. This method provides precise relative photometry in very crowded stellar fields. A stellar catalog was constructed from these reference images by applying DoPHOT (Schechter, Mateo & Saha 1993), the point spread function (PSF)-fitting routine.

Each field is divided into 80 subfields and each subfield is individually calibrated using the RCG feature in each subfield CMD more precisely. About 12% of the area, in which a clear RCG population could not be identified in the CMD, was excluded from the analysis. The number of subfields used in the final analysis is 1536 in total and also given in Table 1 for each field. The coordinates and other properties of the subfields are listed in Table 4.

For the microlensing rate and optical depth estimates, we use two subsamples of events and star counts:

(1) The all-source sample uses stars brighter than  $I_s \leq 20$  mag. This sample contains 474 events. (Sumi et al. 2013) did not require that the events be associated with an apparently resolved reference image star, but did require that the source magnitude is determined from the light curve fit and it is brighter than  $I_s = 20$  mag. Analysis of these samples is less affected by blending, in the same way as previous all source DIA analyses (Sumi et al. 2003; Alcock et al. 2000). However, the analysis requires that the number of sources be counted independently from the event selection.

The GB fields are so crowded that virtually all the main sequence stars are not individually resolved. To count the number of stars with  $I \leq 20$ , Sumi et al. (2013) first estimated the center of RCG  $I$ -band magnitude,  $I_{\text{RC}}$ , and the number of RCG,  $N_{\text{RC}}$ , by fitting the magnitude distribution of the reference images in each subfield with Equation (4) of Nataf et al. (2013). RCG stars are abundant and serve as a good standard candle (Kiraga, Paczyński & Stanek 1997; Stanek et al. 2000) that trace out the density structure of the GB, and hence their numbers should be proportional to the number of all sources.

Sumi et al. (2013) then constructed a combined luminosity function (LF) by using the star catalogs measured in Baade’s Window using the MOA-II reference image for bright stars, and *Hubble Space Telescope* (HST) imaging (Holtzman et al. 1998) for faint stars down to  $I = 24$  mag. This combined LF is calibrated to the extinction and GB distance, and normalized for each subfield so that its  $I_{\text{RC}}$  and  $N_{\text{RC}}$  are same as the values in each

subfield. Then the number of stars  $N_s$  are counted down to  $I = 20$  mag by integrating this scaled-combined LF as shown in Table 1.

The disadvantage of this method is that it assumes that the LF in all fields is the same as that of Baade’s window (Holtzman et al. 1998). The advantage of this method is that it was believed that faint sources can be counted without any problem with blending, because  $N_{\text{RC}}$  is less affected by blending because RCGs are bright. However, below, we show that  $N_{\text{RC}}$  does suffer from incompleteness and that this method is not tolerant against this bias for the measurements of  $\tau$  and  $\Gamma$  because the number of events is not affected by this incompleteness.

(2) The Red Clump Giant (RCG) sample selects only events with  $I_s < 17.5$ , as measured from the lightcurve. To estimate the number of sources, stars in the ”extended RCG region” are counted in the CMD of the reference images as shown in Figure 1 of (Sumi et al. 2013) with  $I_s < 17.5$  mag and the source colors of  $(V - I)_s \geq (V - I)_{\text{RC}} - 0.3$  mag, where  $(V - I)_{\text{RC}}$  is the  $V - I$  color of RCG centroid. There is no color cut on the event selection, but it is assumed that the blue disk sources in front of the bulge have negligible event rate. This process is similar to the OGLE-II optical depth analysis (Sumi et al. 2006) that makes use of the OGLE-II extinction map (Sumi 2004), which is based on the RCG position in the CMD. This contains not only RCGs but also bulge red giants, which is a similar definition to previous works (Alcock et al. 1997; Popowski et al. 2005; Sumi et al. 2006; Hamadache et al. 2006). This sample contains 83 events.

Contrary to previous RCG analyses (Alcock et al. 1997; Popowski et al. 2005; Sumi et al. 2006; Hamadache et al. 2006), Sumi et al. (2013) did not require the event to be associated with an apparently resolved star. So this method is closer to the all source sample analysis above than the previous RCG analyses. Thus their MOA-II RCG analysis is less affected by blending, but affected by the same incompleteness bias as the all-source analysis. On the other hand, incompleteness of the source star count did not affect the previous RCG analyses because the incompleteness in event selection and source count cancel each other out (see more details in § 7).

## 2.2. OGLE Stellar number count

The Optical Gravitational Lensing Experiment (OGLE; Udalski 2003) also conducts a microlensing survey toward the Galactic bulge with the 1.3 m Warsaw telescope at the Las Campanas Observatory in Chile. The median seeing is about 1.3 arcsec. The third phase of OGLE, OGLE-III carried out survey observations with a  $0.36 \text{ deg}^2$  FOV mosaic CCD

camera. Most observations are taken in the standard Kron-Cousin  $I$ -band with occasional observations in the Johnson  $V$ -band.

Nataf et al. (2013) identified RCGs in the CMDs by using OGLE-III photometry maps towards the galactic bulge fields (Szymański et al. 2011)<sup>3</sup> which cover  $-10^\circ < l < 10^\circ$  and  $2^\circ < |b| < 7^\circ$ . Each of the 2104 OGLE-III subfields (eight detectors over 263 fields) used in the work was split into 1, 2, 3, 6, 8, 10, 15, or 21 rectangles depending on the surface density of stars. The average rectangle size is  $6' \times 6'$ . In each rectangle, they estimated the center of the RCG  $I$ -band magnitude,  $I_{\text{RC}}$ , and the number of RCG,  $N_{\text{RC}}$  by fitting the luminosity function with Equation (4) of Nataf et al. (2013).

Thanks to their better seeing and longer exposure than MOA-II, the completeness of the OGLE-III RCG number count is much higher than that of the MOA-II catalog and likely to be almost complete.

### 3. Completeness of the Stellar Number Count

#### 3.1. Comparison to the OGLE RCG number count

We investigate the completeness of the number count of RCGs in the MOA-II GB fields used in Sumi et al. (2013),  $N_{\text{RC},\text{MOA}}$ , by comparing it to that of OGLE-III (Nataf et al. 2013),  $N_{\text{RC},\text{Nataf}}$ .

Figure 1 shows comparison of the number of RCG per subfield ( $98 \text{ arcmin}^2$ ) in MOA ( $N_{\text{RC},\text{MOA}}$ ) at  $|l| < 5^\circ$  and that in OGLE ( $N_{\text{RC},\text{Nataf}}$ ) which are an average over points within 0.085 degrees of the MOA subfield center. One can see that they are consistent at low number density  $N_{\text{RC}} < 1000$ , but as the stellar density increases,  $N_{\text{RC},\text{MOA}}$  becomes systematically lower by up to 30%. This trend is as expected because the completeness depends on the stellar number density, but the magnitude of the difference is significantly larger than anticipated by previous studies, and this could bias the measured  $\tau$  and  $\Gamma$ .

Figure 2 shows the counts as a function of galactic latitude  $b$ . One can see that they are consistent at higher galactic latitude around  $b \sim -6$ , but  $N_{\text{RC},\text{MOA}}$  is systematically fewer than  $N_{\text{RC},\text{Nataf}}$  at lower  $b$  as the number density is higher near the galactic center.

The completeness of RCG counts is expected to depend not only on the number density, but also the RCG magnitude, which depends on the interstellar extinction and the

---

<sup>3</sup><http://ogle.astrouw.edu.pl/>



distance to the galactic bar structure. The top panel of Figure 3 shows the ratio,  $f_{\text{RC}} = N_{\text{RC,MOA}}/N_{\text{RC,Nataf}}$  i.e., the completeness if we assume that  $N_{\text{RC,Nataf}}$  is complete, as a function of the  $I$ -band RCG magnitude measured by Nataf et al. (2013),  $I_{\text{Nataf}}$  and of  $N_{\text{RC,Nataf}}$ . One can see that  $f_{\text{RC}}$  is basically higher for brighter  $I_{\text{Nataf}}$  and smaller  $N_{\text{RC,Nataf}}$  as expected, but the trend is somewhat complicated. The middle and bottom panels of Figure 3 show  $f_{\text{RC}}$  in  $(b, N_{\text{RC,Nataf}})$  and  $(b, I_{\text{RC,Nataf}})$  space, respectively. Both  $N_{\text{RC,Nataf}}$  and  $I_{\text{RC,Nataf}}$  have a clear relation with  $b$ , which explains the clear trend of  $N_{\text{RCs}}$  with  $b$  in Figure 2. In the top and middle panels of Figure 3, one can see that the  $f_{\text{RC}}$  are systematically higher at smaller  $N_{\text{RC,Nataf}}$  at given  $I_{\text{RC,Nataf}}$  and  $b$ . Some fraction of this trend can be attributed to the bias due to the statistical uncertainty of  $N_{\text{RC,Nataf}}$  itself. Because  $f_{\text{RC}}$  is inversely proportional to  $N_{\text{RC,Nataf}}$ ,  $f_{\text{RC}}$  correlates with  $N_{\text{RC,Nataf}}$ .

In order to correct the number counts for incompleteness, we fit for relations between  $f_{\text{RC}}$  as a function of  $N_{\text{RC,Nataf}}$ ,  $I_{\text{RC,Nataf}}$  and  $b$ , which are shown in Figure 4, Figure 5 and the top-left panel of Figure 6, respectively. The scatter in these figures, as well as Figure 1, are about 10%. In principle, if both data sets were equally complete, there should be no scatter between the two. The Poisson uncertainty on the number of stars that are missed in the MOA data is expected to be a few percent. The variation of incompleteness in different subfields can generate additional scatter. We also expect that some scatter is caused by the averaging of Nataf et al.’s subfields in order to match a MOA subfield, together with the fact that the sky covered by the averaged Nataf et al. subfields is not exactly the same as the sky covered by the MOA subfield. Here we perform the linear fits with recursive  $3\sigma$  clipping. In all figures, we can see clear trends. The standard deviations of the residuals for  $N_{\text{RC,Nataf}}$ ,  $I_{\text{RC,Nataf}}$  and  $b$ , after (before)  $3\sigma$  clipping, are 0.10 (0.13), 0.11 (0.14) and 0.10 (0.13), respectively. Thus the relation with  $N_{\text{RC,Nataf}}$  and  $b$  are better than that of  $I_{\text{RC,Nataf}}$ . As the aim of this comparison is to correct the number counts for the completeness, it could bias the result if we use  $N_{\text{RC,Nataf}}$  itself to correct for it, as they have their own uncertainty as mentioned above. Thus we decided to use the relation,

$$f_{\text{RC}} = \frac{N_{\text{RC,MOA}}}{N_{\text{RC,Nataf}}} = (0.63 \pm 0.01) - (0.052 \pm 0.003) \times b. \quad (2)$$

In Figure 6, we also show  $f_{\text{RC}}$  as a function of  $b$  with the galactic longitude of  $|l| \leq 2^\circ$ ,  $2^\circ < |l| \leq 5^\circ$  and  $|l| > 5^\circ$ , respectively. One can see that this relation does not depend on the galactic longitude. So, we apply the relation of Eq. (2) to all subfields.

If there is a significant systematic trend in  $I_{\text{RC,MOA}}$ , then it could also cause a bias in the number count of sources for the all source sample. It is possible that the incompleteness of the RCG mentioned above might bias  $I_{\text{RC,MOA}}$ . We show the differences between  $I_{\text{RC,MOA}}$  and  $I_{\text{RC,Nataf}}$  as a function of  $b$  in Figure 7. One can see that there is a weak trend, while



the amount of the difference due to this slope over the range  $b = -2 \sim -6$  is comparable to the uncertainty in calibration between OGLE and MOA magnitudes which is about  $\sim 0.2$  mag. This difference may also be due to the difference in the filter of MOA and OGLE but it is not clear at this stage. The systematic trend in  $I_{\text{RC}}$  would affect estimates of the event detection efficiency in a complicated way in addition to affecting estimates of the number of sources. To see the magnitude of the bias due to systematics in  $I_{\text{RC}}$ , we calculated the optical depth by correcting the correlation of  $I_{\text{RC},\text{MOA}} - I_{\text{RC},\text{Nataf}} \propto 0.05 \times b$ . We found that the difference from the optical depth results without this correction is a few percent or less than 10% at a maximum. Given the concordance of our updated optical depths with other data sets that would not be affected by this bias, we anticipate that the effect of the bias is smaller than our statistical uncertainties.

Because the reason for the trend in  $I_{\text{RC}}$  is not clear and the effect is relatively small compared to the bias due to the incompleteness on the number count, we correct only for the effect of incompleteness on the number count and not for the effect on  $I_{\text{RC}}$  in the following analysis.

### 3.2. Cause of the Incompleteness

The Nataf et al. (2013) analysis is conservative in order to ensure high completeness. To ensure the completeness in the  $V$ -band, they only consider fields where  $(V - I)_{\text{RC}} \leq 3.30$ , which allows a maximum reddening of  $E(V - I) = 2.24$  with the intrinsic RCG color of  $(V - I)_{\text{RC},0} = 1.06$  (Bensby et al. 2013). The RCGs are more complete in  $I$ -band, which are used for the number count, because they are 3.3 magnitude brighter than in  $V$ -band at this reddening. The OGLE luminosity function of any field shows that the number counts drop off at  $I \sim 20.5$  mag, meaning completeness likely begins to fall at  $I \sim 19$  mag or fainter. In contrast, the maximum reddening of  $E(V - I) = 2.24$  implies  $I_{\text{RC}} = 17.1$  based on the RCGs at 8kpc with the intrinsic  $I$ -band magnitude of  $M_{I,\text{RC},0} = -0.12$  and the average total-to-selective extinction ratio of  $R_I = A_I/E(V - I) = 1.215$  (Nataf et al. 2013). This is substantially brighter than the estimated completeness cutoff.

For the RCG number count, Nataf et al. (2013) used stars with  $V - I \geq (V - I)_{\text{RC}} - 0.3$  and  $-1.5 < I - I_{\text{RC}} < 1.5$ . They included stars without  $V$ -band photometry assuming that they are fainter in  $V$ -band, i.e., redder than the limit  $(V - I)_{\text{RC}} - 0.3$ . Thus their number count is not affected by the incompleteness in  $V$ -band.

On the other hand, there are some reasons for the incompleteness of RCG number count in MOA-II analysis by Sumi et al. (2013). The major reason is the incompleteness in  $V$ -

band catalog compiled using DOPHOT. The limiting magnitude in  $I$ -band is  $I \sim 18.3$  mag which is still deeper than the  $I$ -band RCG magnitude of  $I_{\text{RC}} = 17.1$  with the reddening of  $E(V - I) = 2.24$  given above, which is roughly equivalent to or slightly lower than the maximum reddening in MOA-II fields. However,  $V$ -band limiting magnitude is about  $V \sim 20.3$  mag, which is comparable to the  $V$ -band RCG magnitude of  $V_{\text{RC}} = 20.4$  with  $E(V - I) = 2.24$ , i.e.,  $A_V = 4.96$  by using  $R_I = A_I/E(V - I) = 1.215$  (Nataf et al. 2013).

Sumi et al. (2013) computed the RCG number count using stars selected with a similar color and magnitude limit as OGLE,  $I < 17.5$  mag,  $V - I \geq (V - I)_{\text{RC}} - 0.3$  as shown in their Figure 1. However, stars without  $V$ -band photometry were not included. Thus the incompleteness in  $V$ -band catalog affects the number count.

We conclude that the RCG number count in MOA-II was not optimized for this purpose. There are some ways to avoid this problem in future analysis for MOA-II. For example, (1) get deeper  $V$ -band images, (2) Include all stars without a  $V$ -band detection following Nataf et al. (2013), (3) Use the OGLE number count instead.

#### 4. Microlensing Optical Depth and Event Rate

Here we have re-calculated the microlensing optical depth and event rate by following Sumi et al. (2013), but using the stellar number count corrected for the completeness by Eq.(2).

The optical depth,  $\tau$ , can be calculated by using Eq. (1). The microlensing event rate per star per year,  $\Gamma$ , can be determined observationally from the following expression,

$$\Gamma = \frac{1}{N_s T_o} \sum_i \frac{1}{\varepsilon(t_{\text{E},i})}, \quad (3)$$

Here we use the detection efficiency determined by Sumi et al. (2011). In our event rate and optical depth analyses for this 2006-2007 data set,  $T_o = 596.0$  days and the corrected number of source stars is (1)  $N_* = 110.3 \times 10^6$  for the all-source sample and (2)  $N_{*,\text{RC}} = 8.00 \times 10^6$  for the RCG sample.

Individual optical depth estimates for all sources in each field are listed in Table 1. The upper panel of Figure 8 shows a smoothed map of optical depth of each subfield in Galactic coordinates. The plotted values from all subfields are listed in Table 4 of the online version, with a sample of this table listed in the printed version of this paper. The smoothing is done with a Gaussian function with  $\sigma = 0.4^\circ$ , and cut off at a distance of  $1^\circ$  from the center of each subfield. The error bars for each subfield are estimated with the bootstrap method

of Alcock et al. (1997), using the neighboring subfields with the same weighting as in the calculation of the central values.

We also estimated the average optical depth in all fields combined, and found  $\tau_{200} = 1.53^{+0.12}_{-0.11} \times 10^{-6}$  with 474 events for all source sample and  $\tau_{200} = 1.28^{+0.27}_{-0.19} \times 10^{-6}$  with 83 events for RCG sample at  $(l, b) = (1.^{\circ}85, -3.^{\circ}69)$ . These are reductions of 18 and 19 percent, respectively, or  $2.6\sigma$  and  $1.3\sigma$ , respectively. The effective line of sight was computed by weighting the number of subfields used. The errors were estimated using the bootstrap Monte-Carlo method of Alcock et al. (1997).

## 5. Modeling the Optical Depth Results

The optical depth given by Equation (1) does not follow Poisson statistics because each event is summed with an unequal weight of  $t_{E,i}/\varepsilon(t_{E,i})$ . Therefore, we binned the optical depth values of the subfields in order to model the optical depth distribution.

Figure 9 shows the optical depth,  $\tau_{200}$ , as a function of  $b$  for both the all-source sample and RCG samples for the central region with  $|l| < 5^{\circ}$ , chosen so as to overlap with previous measurements. The subfield results are binned with a bin width of  $\Delta b = 0.5^{\circ}$ . The binned values for the all-source and RCG samples are given in Tables 2 and 3, respectively.

The optical depth clearly increases with decreasing  $|b|$ , and a simple exponential fit gives,  $\tau_{200} = [1.84 \pm 0.14] \times 10^{-6} \exp[(0.44 \pm 0.07)(3 - |b|)]$  for the all-source sample as indicated by the black solid line in Figure 9. This is a significantly lower and shallower slope than the original result of  $\tau_{200} = [2.35 \pm 0.18] \times 10^{-6} \exp[(0.51 \pm 0.07)(3 - |b|)]$  estimated by Sumi et al. (2013) before correcting the completeness of the RCG number count. The exponential model still represents the data well.

This result is significantly smaller than the measurements by MOA-I (Sumi et al. 2003) and MACHO (Alcock et al. 2000) with all-source samples. Contrary to the original measurements, it is very consistent with the RCG measurements by MACHO (Popowski et al. 2005), EROS-2 (Hamadache et al. 2006) and OGLE-II (Sumi et al. 2006). The best linear fit to the OGLE-II RCG measurements is indicated by the red dashed line in Figure 9 as a comparison.

The MACHO (Popowski et al. 2005) and EROS (Hamadache et al. 2006) analyses identified microlensing events solely by their proximity to apparent RCG stars identified in the reference images, with no attempt to determine if the source is a RCG star or a blended fainter main sequence star. These blending effects will shrink apparent  $t_E$  values for all

events, while increasing the number of apparent RCG events. Popowski et al. (2005) and Hamadache et al. (2006) make arguments to suggest that these two effects approximately cancel.

The only previous RCG sample that distinguished RCG source events from events with main sequence sources that happened to be blended with RCG stars was the OGLE-II analysis of Sumi et al. (2006). I.e., they are less affected by blending than the above MACHO and EROS RCG analyses. The one similarity of their RCG analysis with other RCG analyses is that they require that events to be associated with resolved stars. Their OGLE-II value is consistent with MACHO and EROS RCG analyses. Thus it is likely that this cancellation of shrinking  $t_E$  and increasing the number of events, works to within the accuracy presented in their analyses, as confirmed by image level simulation by Smith, Woźniak, Mao & Sumi (2007).

An exponential fit for the optical depth toward RCG sources gives  $\tau_{200} = [1.28 \pm 0.21] \times 10^{-6} \exp[(0.40 \pm 0.17)(3 - |b|)]$ , which is indicated by the red solid line in the Figure 9. This is also significantly lower than the original estimate and previous RCG measurements (Popowski et al. 2005; Sumi et al. 2006; Hamadache et al. 2006) and some older bulge models (Bissantz & Gerhard 2002; Han & Gould 2003; Kerins, Robin & Marshal 2009).

However, in this particular analysis, this  $\tau$  estimate for the RCG sample is heavily biased by the low detection efficiency for events with  $t_E > 100$  days, due to the fact that the analysis was originally designed to focus on short time scale events. Although the events with  $t_E < 200$  days are selected, most of the events with  $t_E > 100$  days with bright sources could not satisfy the requirement for a long enough constant baseline. This is because the tails of the events are longer than  $t_E$  and they are still significantly above the baseline for bright source events. This effect is negligible for the all source sample. Thus we can not directly compare this result with other measurements.

## 6. Modeling the Event Rate

The event rate per square degree per year,  $\Gamma_{\text{deg}^2}$ , for source stars above a magnitude threshold of  $I_s \leq 20$ , which are given in Table 1-4 for completeness, does not change from Sumi et al. (2013) because this quantity is independent of the stellar number count. Thus, we focus on the event rate per star per year,  $\Gamma$ , in the rest of the paper.

We model the event rate,  $\Gamma$  by using the Poisson statistics fitting method, first introduced by Sumi et al. (2013). This method allows us to fit to the raw, subfield data, even though the average number of events per subfield is  $< 1$ , thus free from the problem on the

binning of the sample and the improper assumption of the gaussian statistics. The number of expected events in a subfield is given by

$$N_{\text{ev,exp}}(l, b) = \Gamma_{\text{mod}}(l, b) N_{\text{s}}(l, b) T_{\text{o}} \langle \varepsilon(l, b) \rangle , \quad (4)$$

where  $N_{\text{s}}$  is the number of stars in the subfield, and  $\langle \varepsilon(l, b) \rangle$  is the detection efficiency averaged over  $t_{\text{E}}$  for the subfield at coordinates  $(l, b)$ . We adopt the average detection efficiency given in Tables 2 and 3 of Sumi et al. (2013), for the all-star and RCG samples, respectively, while  $N_{\text{s}}$  need to be corrected by Eq. (2).

The probability of the observed number of events,  $N_{\text{ev}}(l, b)$ , in the subfield at  $(l, b)$  is

$$P[N_{\text{ev}}(l, b)] = \frac{e^{-N_{\text{ev,exp}}(l, b)} N_{\text{ev,exp}}(l, b)^{N_{\text{ev}}(l, b)}}{N_{\text{ev}}(l, b)!} , \quad (5)$$

according to Poisson statistics. We can then define the  $\chi^2$  by,  $\chi^2 = -2 \sum_{(l, b)} \ln P[N_{\text{ev}}(l, b)]$ .

Thus the event rate,  $\Gamma$ , is the preferred quantity to compare to Galactic models rather than the optical depth. We show the event rate per star per year  $\Gamma$  and the exponential fits for the all-source and RCG samples as a function of the galactic latitude,  $b$ , for  $|l| < 5^\circ$  in Figure 10 and in Tables 2 and 3, respectively. The event rate has much less scatter than  $\tau_{200}$  and  $\Gamma$  for both the all-source and RCG samples, and both are well fit by a simple exponential model. Note that these fits are done to the subfield data using the Poisson statistics method, while the plots show binned quantities for display in Figure 10 and in Tables 2 and 3.

The exponential model for the all-source and RCG samples are quite similar with  $\Gamma_{\text{all}} = [18.74 \pm 0.91] \times 10^{-6} \exp[(0.53 \pm 0.05)(3 - |b|)] \text{ star}^{-1} \text{ yr}^{-1}$  for the all-source sample and  $\Gamma_{\text{RC}} = [17.13 \pm 2.03] \times 10^{-6} \exp[(0.58 \pm 0.12)(3 - |b|)] \text{ star}^{-1} \text{ yr}^{-1}$  for the RCG sample. Again, due to the  $N_{\text{s}}$  correction, these have a smaller and shallower slope than the original values in Sumi et al. (2013). The RCG event rate is slightly smaller, but consistent with the all-source event rate. The RCG slope is  $0.4\sigma$  steeper and the amplitude is 8% or  $0.8\sigma$  smaller. As noted earlier, this is because  $\Gamma$  is much less sensitive to the bias due to the small number of long  $t_{\text{E}}$  events.

Sumi et al. (2013) noted that although there is a possible problem with assuming the luminosity function in all other fields are same as the *HST* luminosity function measured in Baade’s window (Holtzman et al. 1998), the uncertainty due to the different luminosity function shape would largely cancel out if the same luminosity function is used in the detection efficiency simulations and the source star counts. The consistency between the all-source and RCG  $\Gamma$  values indicates that the effect due to the variation of the luminosity function shape in each field relative to the *HST* luminosity function are negligible. However, they were not

aware that the effect on the normalization of the luminosity function is more significant than its shape.

We show exponential fits as a function of the galactic latitude  $b$  for  $\tau_{200}$  and  $\Gamma$  for different bins in Galactic longitude,  $l$  in Figures 11 and 12, respectively. The black points and curves are for all the events with  $-2^\circ.25 < l < 3^\circ.75$ . In Figure 12, it provides a reasonable fit to all the longitude bins, except the  $0^\circ.75 < l < 2^\circ.25$  bin, where there is an enhancement to the rate. On the other hand, there is some scatter in  $\tau_{200}$  between different bins in Figure 11. The  $\tau_{200}$  bin with  $0^\circ.75 < l < 2^\circ.25$  at small  $|b|$  is smaller than the average, which is different from  $\Gamma$ . This is because average  $t_E$  is smaller at these galactic central regions due to the galactic kinematics as shown in Fig. 3 of Sumi et al. (2013).

Figure 8 shows smoothed maps of  $\tau_{200}$  and  $\Gamma$  in Galactic coordinates. The plotted values from all subfields are listed in Table 4. The smoothing is done with a Gaussian function with  $\sigma = 0.4^\circ$ , and cut off at a distance of  $1^\circ$  from the center of each subfield. The error bars for each subfield are estimated using a bootstrap method using the neighboring subfields with the same weighting as in the calculation of the central values. They are similar to the original maps in Fig. 3 of Sumi et al. (2013), but decreased by up to  $\sim 40\%$  depending on  $b$ . The highest optical depth is found at  $l \approx 3^\circ$  and this is due to the excess of long timescale events at this longitude, and could be due to the statistical fluctuations enhanced by large weight for long events.

The event rate per star,  $\Gamma$  has a peak at  $l \approx 1^\circ$ . Because these event rate measurements obey Poisson statistics, the statistical uncertainty in  $\Gamma$  is smaller than the uncertainty in  $\tau_{200}$ . So, we expect that this  $l \approx 1^\circ$  enhancement in the microlensing rate is real and that it is related to the structure and kinematics of the bulge.

As a comparison to Sumi et al. (2013), we have fit  $\Gamma$  with a 16-parameter model in  $l$  and  $b$ . The 16 parameters consist of a 10-parameter cubic polynomial and the inverse of a 6-parameter quadratic polynomial. That is

$$\begin{aligned} \Gamma = & a_0 + a_1 l + a_2 b + a_3 l^2 + a_4 l b + a_5 b^2 + a_6 l^3 + a_7 l^2 b + a_8 l b^2 + a_9 b^3 \\ & + 1/(a_{10} + a_{11} l + a_{12} b + a_{13} l^2 + a_{14} l b + a_{15} b^2) . \end{aligned} \quad (6)$$

The best fit model is shown in Figure 13 and the model parameters are listed in Table 5. The model has a maximum at  $l \approx 1^\circ$  that was also evident in Figure 8.

## 7. Discussion and conclusions

We examined the completeness of the stellar number count in the measurement of the microlensing optical depth  $\tau$  and event rate per star per year  $\Gamma$  toward the Galactic bulge from the first two years of the MOA-II survey (Sumi et al. 2013). We found a significant incompleteness in MOA-II’s RCG counts, which is proportional to the galactic  $b$ . The completeness ranges from 1 to 0.7 for  $b = -6^\circ \sim -1.5^\circ$ . The counts are less complete at lower  $|b|$  because of the higher stellar number density and the higher interstellar extinction. This incompleteness caused the overestimates in the  $\tau$  and  $\Gamma$ .

By correcting this incompleteness, we estimated  $\tau$  and  $\Gamma$  with the all source sample of 474 events and a RCG sample of 83 events. Note that our RCG optical depth is known to be biased low, due to the low efficiency for long duration bright events. Thus we focus on  $\tau$  with all source sample in the following discussion. Due to this correction of the incompleteness, both  $\tau$  and  $\Gamma$  decreased at lower  $|b|$ . This result may have solved the previously noted difference between the optical depths measured with RCG samples (Popowski et al. 2005; Sumi et al. 2006; Hamadache et al. 2006) and that with faint source samples from DIA (Alcock et al. 2000; Sumi et al. 2003), for which the faint source analyses have shown systematically higher  $\tau$  values.

The original measurement of  $\tau$  with all source by MOA-II (Sumi et al. 2013) were in-between of the other previous measurements with all-source and RCG sample and consistent within 1 or 2- $\sigma$  level. Thus they concluded that the previously seen difference between the all-source and RCG samples was due to statistical fluctuations.

However, our revised all-source optical depth measurements are consistent with previous measurements for RCG samples and significantly lower than that of the Sumi et al. (2013) all-source sample as shown in Figure 9. We can use the exponential models shown in Figure 9 to interpolate our measurement to the center of previous samples. For the MACHO DIA all-source result at  $b = -3^\circ.35$  (Alcock et al. 2000), we find  $\tau_{200} = [1.58 \pm 0.13] \times 10^{-6}$  which is 2.1- $\sigma$  smaller than the MACHO result of  $\tau_{180} = 2.43^{+0.39}_{-0.38} \times 10^{-6}$ . The MOA-I all-source result (Sumi et al. 2003), centered at  $b = -3^\circ.8$ , is  $\tau_{150} = 2.59^{+0.84}_{-0.64} \times 10^{-6}$ . This compares to our interpolated value of  $\tau_{200} = [1.29 \pm 0.11] \times 10^{-6}$ , which is 1.7- $\sigma$  smaller. Thus, our revised optical depth measurement is smaller at the  $\sim 2$ - $\sigma$  level than both the previous all-source measurements, which suggests that these measurements also suffer the same bias in the stellar number count. Because Alcock et al. (2000); Sumi et al. (2003) used the similar method as this work, it is very likely that they have similar bias.

The MACHO Collaboration published several averages of their results (Popowski et al. 2005), but we compare to their “CGR+3” average of  $6 \text{ deg}^2$  centered at  $b = -2^\circ.73$ . MACHO



reports  $\tau_{500} = 2.37^{+0.47}_{-0.39} \times 10^{-6}$  for RCG sources at this position. This compares to our interpolated all-source value of  $\tau_{200} = [2.08 \pm 0.17] \times 10^{-6}$ , which is just 0.6- $\sigma$  smaller.

The RCG sample of the EROS Collaboration (Hamadache et al. 2006) covers a slightly larger area than the MOA-II analysis. They fit their results to an exponential model that is identical to the one shown in Figure 9, and they find  $\tau_{400} = [1.62 \pm 0.23] \times 10^{-6} \exp[(0.43 \pm 0.16)(3 - |b|)]$ . This has a slope that is consistent with our fits, so we compare the results by simply comparing the normalization parameters. Our normalization parameter is  $[1.84 \pm 0.14] \times 10^{-6}$ , which is 0.8- $\sigma$  larger than the EROS value of  $[1.62 \pm 0.23] \times 10^{-6}$ . A more fair comparison would be to compare to the the EROS fit to a model fit to all our fields, instead of just those with  $|l| < 5^\circ$ . This gives  $\tau_{200} = [1.74 \pm 0.13] \times 10^{-6} \exp[(0.45 \pm 0.07)(3 - |b|)]$ , which is 0.4- $\sigma$  larger than the EROS value.

The OGLE-II RCG analysis (Sumi et al. 2006) found  $\tau_{400} = 2.55^{+0.57}_{-0.46} \times 10^{-6}$  at  $b = -2^\circ.75$  which is consistent with other RCG analyses. This compares to our all-source result, interpolated from the model given in Figure 9, is  $\tau_{200} = [2.06 \pm 0.17] \times 10^{-6}$ , which is just 0.9- $\sigma$  smaller.

In summary, we find that our all-source results are about 2- $\sigma$  smaller than the previous all-source measurements, and they are very consistent with the RCG optical depth values from OGLE, MACHO and EROS within 1- $\sigma$ .

Note that the observed optical depths mentioned above represent the contributions of optical depth from the events within the given timescale range. The upper limit of the  $t_E$  in these analyses range between 150-500 days. However, the longest  $t_E$  detected in their sample is mostly less than 200 days and the contributions of  $\tau$  from the events with  $t_E > 150$  days are negligible. Thus above comparison is valid within the their uncertainty.

We compare the optical depth results with values predicted from the models. Han & Gould (2003) model predicts  $\tau = [1.63 \pm 0.13] \times 10^{-6}$  at  $b = -3^\circ.9$ , where our all-source optical depth  $\tau_{200} = [1.24 \pm 0.10] \times 10^{-6}$  is 3.9- $\sigma$  smaller. The values from Wood & Mao (2005) models are  $\tau = 2.1 \times 10^{-6}$  at  $b = -3^\circ$  and  $\tau = 3.0 \times 10^{-6}$  at  $b = -2^\circ$ . Our values  $\tau_{200} = [1.84 \pm 0.15] \times 10^{-6}$  and  $\tau_{200} = [2.87 \pm 0.24] \times 10^{-6}$  agree with them with 1.7- $\sigma$  and 0.5- $\sigma$ , respectively. Evans & Belokurov (2002) present a number of models, and the value of their “Dwek plus spiral structure” model  $\tau = 1.5 \times 10^{-6}$  at  $b = -3.8^\circ$  agrees with our  $\tau_{200} = [1.29 \pm 0.11] \times 10^{-6}$  which is 1.9- $\sigma$  smaller, while their other models predict much higher optical depths. The models of Bissantz & Gerhard (2002) predict  $\tau = 1.1 \times 10^{-6}$  at  $b = -3.35^\circ$  for all sources and  $\tau = 1.3 \times 10^{-6}$  at  $b = -3.8^\circ$  for RCG sources. Our values  $\tau_{200} = [1.58 \pm 0.13] \times 10^{-6}$  and  $\tau_{200} = [1.29 \pm 0.11] \times 10^{-6}$  are 3.7- $\sigma$  and 0.2- $\sigma$  larger, respectively. Kerins, Robin & Marshal (2009)’s model predicts  $\tau = 4 \times 10^{-6}$  at  $b = -1^\circ.9$  and

$\tau = 2 \times 10^{-6}$  at  $b = -3^\circ.5$ , where our measurements are  $\tau_{200} = [3.00 \pm 0.25] \times 10^{-6}$  and  $\tau_{200} = [1.48 \pm 0.12] \times 10^{-6}$  which are  $4.0\text{-}\sigma$  and  $4.3\text{-}\sigma$  smaller, respectively.

As discussed above in Section 6 and shown in Figures 8 and 10,  $\Gamma$  can be measured more precisely than  $\tau$ . Furthermore,  $\tau$  has an additional systematic uncertainty due to potential very long time scale events, which may contribute significantly to  $\tau$  but not to  $\Gamma$ . Figure 10 indicates that the all-source and RCG  $\Gamma$  values differ by only less than 9%.

Recently, Awiphan, Kerins & Robin (2016) presented the field-by-field comparison between results by Sumi et al. (2013) and the Besançon population synthesis Galactic model. They found only  $\sim 50\%$  of the measured  $\tau$  and event rate per star per year,  $\Gamma$ , at low Galactic latitude around the inner bulge ( $|b| < 3^\circ$ ) and suggested the discrepancy most likely is associated with known underestimated extinction and star counts in the innermost regions, which supports missing inner stellar population. Here we compared their model and our revised  $\tau$  and  $\Gamma$ , in Fig. 14 and 15, respectively. Their model is more consistent with our revised  $\tau$  than the original measurements by Sumi et al. (2013), but are still slightly higher. The difference is not very significant due to the large error in our measurement. Our revised  $\Gamma$  are very consistent to their model without any missing inner stellar population.

Sumi et al. (2013) noted a possible problem with assuming that the luminosity function in all fields are same as the *HST* luminosity function in Baade’s window (Holtzman et al. 1998). However, the consistency between the all-source and RCG  $\Gamma$  values indicates that the effect due to the variation of the luminosity function shape in each field from the *HST* luminosity function are negligible.

However, Sumi et al. (2013) were not aware that the completeness of the number counts of RCGs might be problematic, because they were thought to be bright enough to be complete. In their analyses for both all source sample and RCG sample, the stellar number count is based on the stellar catalog in the reference images reduced by DoPHOT (Schechter, Mateo & Saha 1993) algorithm, where the combined ground+HST luminosity function are normalized by the RCG number counts and the events were selected regardless of whether they are associated with resolved stars. Thus, both samples are biased by the same amount. This incompleteness is mostly because MOA-II data was taken under relatively poor seeing of  $\sim 1.8$  arcsec even in the reference images. The measurements by MOA-I (Sumi et al. 2003) and MACHO (Alcock et al. 2000) also used a similar method with similar seeing, and are therefore expected to suffer the same problem.

Other measurements using RCG samples by OGLE-II (Sumi et al. 2006), MACHO (Popowski et al. 2005) and EROS (Hamadache et al. 2006) used a different method, which selected only the events at the position of the resolved stars in the reference image by

DoPHOT or similar algorithm. Thus, the incompleteness affects both the number of events and stellar number count, thus they cancel each other out.

In conclusion, we believe the long-standing problem of the discrepancy between the high optical depth in all source sample by DIA and low optical depth with RCG sample can be explained by the incompleteness of the stellar number count.

These measurements of  $\Gamma$  and  $\tau$  have the highest spatial resolution so far thanks to our samples being the largest studied so far. Our goal is to measure  $\Gamma$  and  $\tau$  precisely around the galactic bulge to constrain the barred Galactic bulge model. Currently MOA-II and OGLE-IV detect about 700 and 2,000 events a year, respectively. In the near future, this analysis will be expanded by thousands of events.

Another goal of this work is to predict the event rate in the inner Galactic bulge for the future space microlensing survey of the Wide Field Infrared Space Telescope (WFIRST) (Green et al. 2012; Spergel et al. 2015) and Euclid (Penny et al. 2013). The expected microlensing event rate for the WFIRST mission is uncertain because the region with the highest event rate at low Galactic latitudes are not well studied due to the high interstellar extinction. This work provides the best estimate of the event rate in the inner Galactic bulge to date. For  $3.2 \text{ deg}^2$  of the MOA-II survey area inside  $|b| \leq 3^\circ.0$  and  $0^\circ.0 \leq l \leq 2^\circ.0$ , centered at  $(l, b) = (0.^\circ97, -2.^\circ26)$ , we find  $\Gamma = 3.41^{+0.38}_{-0.34} \times 10^{-5} \text{ star}^{-1} \text{ yr}^{-1}$  for sources with  $I < 20$ . This is consistent with the rate model used for the report of the WFIRST Science Definition Team (SDT) (Green et al. 2012; Spergel et al. 2015) evaluated at this position, while the previous value was a factor 1.3 larger than this. By extrapolating to the lower latitude fields,  $|b| \sim -1^\circ.4$ , where the WFIRST will observe, the model with  $-2^\circ.25 < l < 3^\circ.75$  presented in Figure 12 predicts  $\Gamma = 4.60 \pm 0.25 \times 10^{-5} \text{ star}^{-1} \text{ yr}^{-1}$  for sources with  $I < 20$ , which is consistent with the value in the WFIRST SDT report.

In this work, we have attempted to correct for incompleteness by assuming that another data set is complete, when that data set itself has not been corrected for completeness (Nataf et al. 2013). While we expect OGLE number counts to be more complete than MOA's, it was long assumed that completeness would not be an issue for MOA. This is of course not ideal, but was done so for the sake of expediently correcting a significant systematic error. Instead, in future, it would be better for all studies that fit models to number counts of bulge RCG stars to first correct for incompleteness using artificial star tests. Without doing so it is possible that models fit to the magnitude distribution around the red clump might systematically underestimate the number of stars, as well as the location of the clump if the incompleteness varies as a function of magnitude (which it almost certainly does). Failure to do so could impact studies of galactic structure (e.g. Rattenbury et al. 2007; Cao et al. 2013; Wegg & Gerhard 2013), interstellar extinction (Sumi 2004; Nataf et al. 2013; Gonzalez et al.

2011) and as we have shown here, microlensing event rates and optical depths.

TS acknowledges the financial support from the JSPS, JSPS23340044, JSPS24253004. Work by MTP was performed under contract with the California Institute of Technology (Caltech)/Jet Propulsion Laboratory (JPL) funded by NASA through the Sagan Fellowship Program executed by the NASA Exoplanet Science Institute.

## REFERENCES

- Afonso, C. et al. 2003, *A&A*, 404, 145
- Alard C., 2000, *A&AS*, 144, 363
- Alard C., Lupton R. H., 1998, *ApJ*, 503, 325
- Alcock, C. et al. 1997, *ApJ*, 486, 697
- Alcock C. et al., 2000b, *ApJ*, 541, 734
- Awiphan, S., Kerins, E. & Robin, A. C., 2016, *MNRAS*, 456, 1666
- Bennett, D.P. & Rhie, S.H. 2002, *ApJ*, 574, 985
- Bensby, T., Yee, J. C., Feltzing, S., et al. 2013, *A&A*, 549, A147
- Bissantz, N. & Gerhard, O. 2002, *MNRAS*, 330, 591
- Bond I. A. et al., 2001, *MNRAS*, 327, 868
- Cao, L., Mao, S., Nataf, D., Rattenbury, N. J., & Gould, A., 2013, *MNRAS*, 434, 595
- Evans N.W., & Belokurov, 2002, *ApJ*, 567, 119
- Gonzalez, O. A., Rejkuba, M., Zoccali, M., Valenti, E., & Minniti, D. 2011, *A&A*, 534, A3
- Gould, A. & An, J. H. 2002, *ApJ*, 565, 1381
- Green, J. et al., 2012, preprint, astro-ph/1208.4012
- Griest, K., et al. 1991, *ApJ*, 372, L79
- Gyuk, G. 1999, *ApJ*, 510, 205
- Hamadache, C., Le Guillou, L., Tisserand, P., et al. 2006, *A&A*, 454, 185

- Han, C. & Gould, A. 1995, *ApJ*, 449, 521
- Han, C. & Gould, A. 2002, *ApJ*, 592, 172
- Han, C. 1999, *MNRAS*, 309, 373
- Holtzman, J. A., Watson, A. M., Baum, W. A., et al. 1998, *AJ*, 115, 1946
- Kerins, E., Robin, A. C., & Marshal, D. J. 2009, *MNRAS*, 396, 1202
- Kim, S.-L., Park, B.-G., Lee, C.-U., et al. 2010, *Proc. SPIE*, 7733, 77333F
- Kiraga, M., & Paczyński, B. 1994, *ApJ*, 430, L101
- Kiraga, M., Paczyński, B. & Stanek, K. Z., 1997, *ApJ*, 485, 611
- Nataf, D. M. et al. 2013, *ApJ*, 769, 88
- Novati S.C., Luca, F. De., Jetzer, Ph., Mancini, L., & Scarpetta, G. 2008, *A&A*, 480, 723
- Paczynski, B. 1986, *ApJ*, 304, 1
- Paczynski, B. 1991, *ApJ*, 371, L63
- Paczynski, B. et al. 1994, *ApJ.*, 435, L113
- Paczynski, B. 1996, *ARA&A*, 34, 419
- Peale, S. J. 1998, *ApJ*, 509, 177
- Penny, M. T., Kerins, E., Rattenbury, N. J., et al. 2013, *MNRAS*, 434, 2
- Popowski, P. et al. 2001, in *ASP Conference Series: Microlensing 2000: A New Era of Microlensing Astrophysics*, eds. J.W. Menzies & P.D. Sackett (San Francisco: Astronomical Society of the Pacific), Vol. 239, p. 244, (astro-ph/0005466)
- Popowski, P. et al. 2005, *ApJ*, 631, 879
- Rattenbury, N.J., Mao, S., Sumi, T., & Smith, M. C. 2007, *MNRAS*, 378, 1064
- Sako, T., et al. 2008, *Experimental Astronomy*, 22, 51
- Schechter, L., Mateo, M., & Saha, A., 1993, *PASP*, 105, 1342S
- Shvartzvald, Y., & Maoz, D. 2012, *MNRAS*, 419, 3631
- Smith, M. C., Woźniak, P. R., Mao, S. & Sumi, T., 2007, *MNRAS*, 380, 805

- Spergel, D. et al., 2015, preprint, astro-ph/1503.03757
- Stanek, K. Z. et al. 2000, *Acta Astronomica*, 50, 191
- Sumi, T., 2004, *MNRAS*, 349, 193
- Sumi, T. et al., 2003, *ApJ*, 591, 204
- Sumi, T. et al., 2006, *ApJ*, 636, 240
- Sumi, T. et al., 2011, *Nature*, 473, 349
- Sumi, T. et al., 2013, *ApJ*, 778, 150
- Szymański, M. K., Udalski, A., Soszyński, I., et al. 2011, *AcA*, 61, 83
- Tomany, A. B. & Crotts, A. P., 1996, *AJ*, 112, 2872
- Udalski, A. et al. 1994, *Acta Astronomica*, 44, 165
- Udalski A. et al. 2002, *Acta Astronomica*, 52, 217
- Udalski, A. 2003, *Acta Astronomica*, 53, 291
- Wegg, C. & Gerhard, O. 2013, *MNRAS*, 435, 1874
- Wood, A., & Mao, S. 2005, *MNRAS*, 362, 945
- Woźniak P. R., & Paczyński, B. 1997, *ApJ*, 487, 55
- Woźniak, P. R., et al. 2001, *Acta Astronomica*, 51, 175
- Zhao, H. & Mao, S. 1996, *MNRAS*, 283, 1197
- Zhao, H., Spergel, D. N. & Rich, R. 1995, *ApJ*, 440, L13

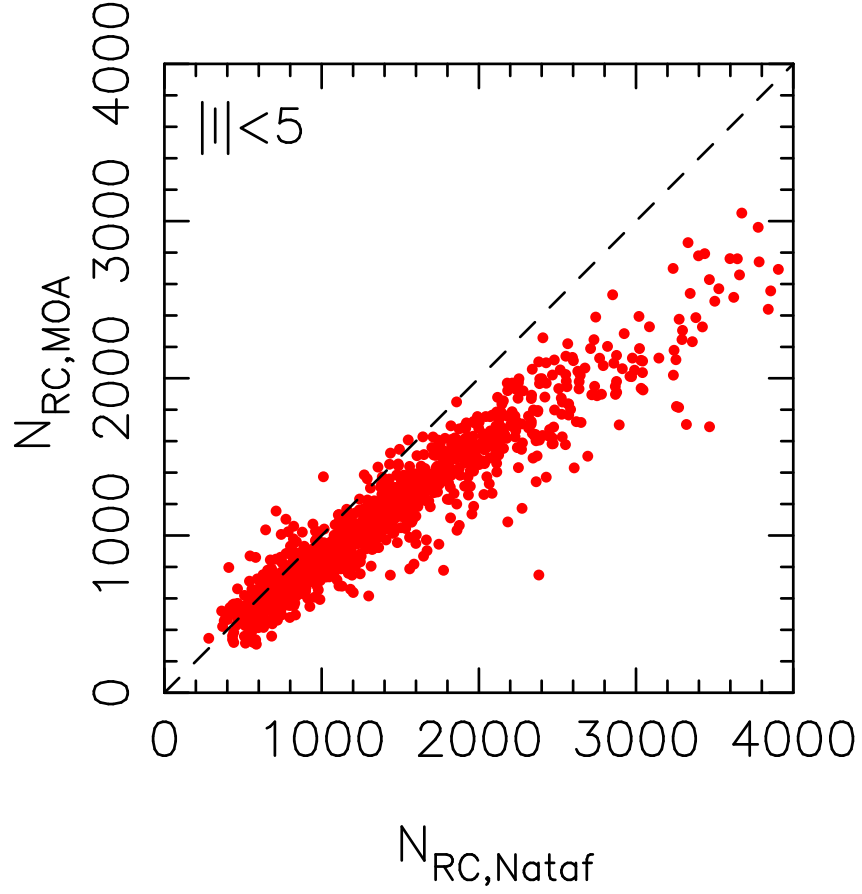


Fig. 1.—: The comparison of the number of red clump giants (RCG) per subfield ( $98 \text{ min.}^2$ ) in MOA,  $N_{\text{RC},\text{MOA}}$  and the that in OGLE,  $N_{\text{RC},\text{Nataf}}$ , which are an average over points within  $0.085$  degrees of the MOA subfield center.



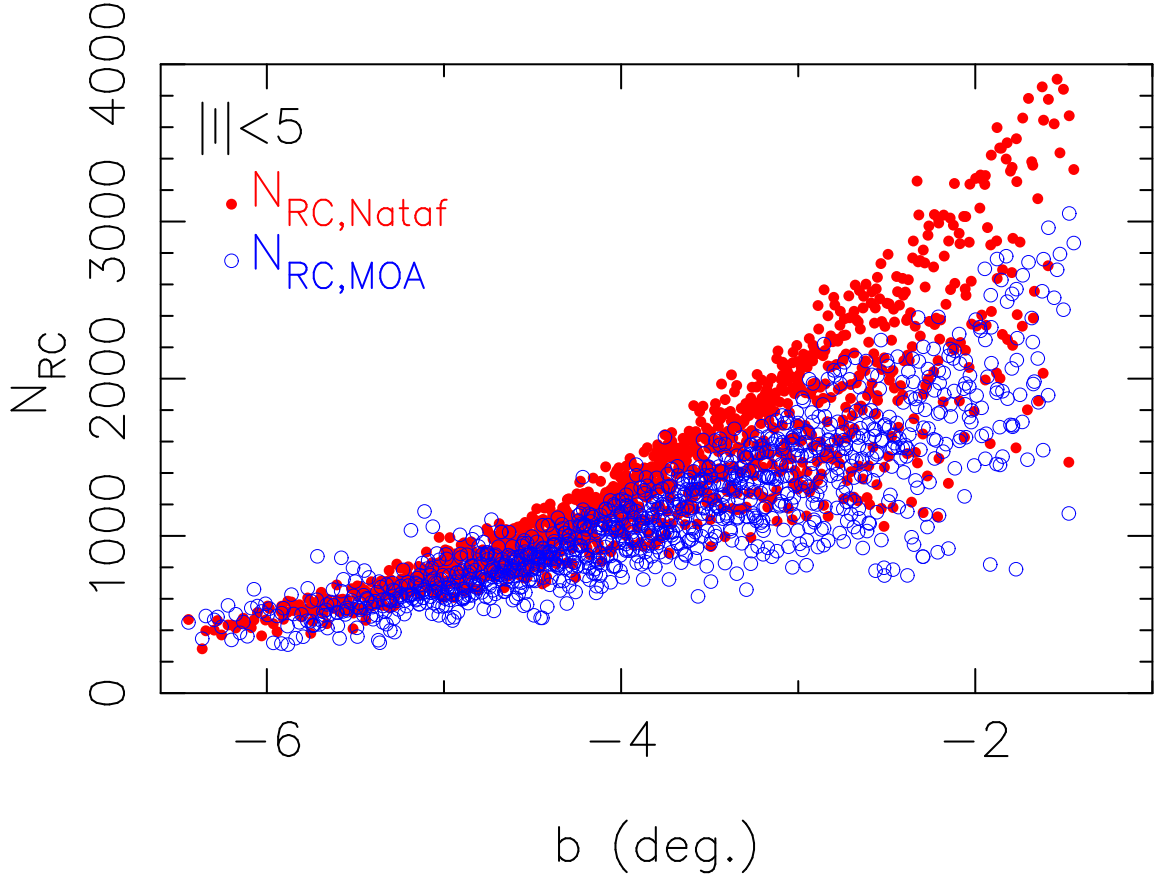


Fig. 2.—: The number of RCG per subfield ( $98 \text{ arcmin}^2$ ) in MOA ( $N_{\text{RC,MOA}}$ , blue open circle) and that in OGLE ( $N_{\text{RC,Nataf}}$ , red filled circle) which are an average over points within  $0.085$  degrees of the MOA subfield center, as a function of the galactic latitude  $b$ .

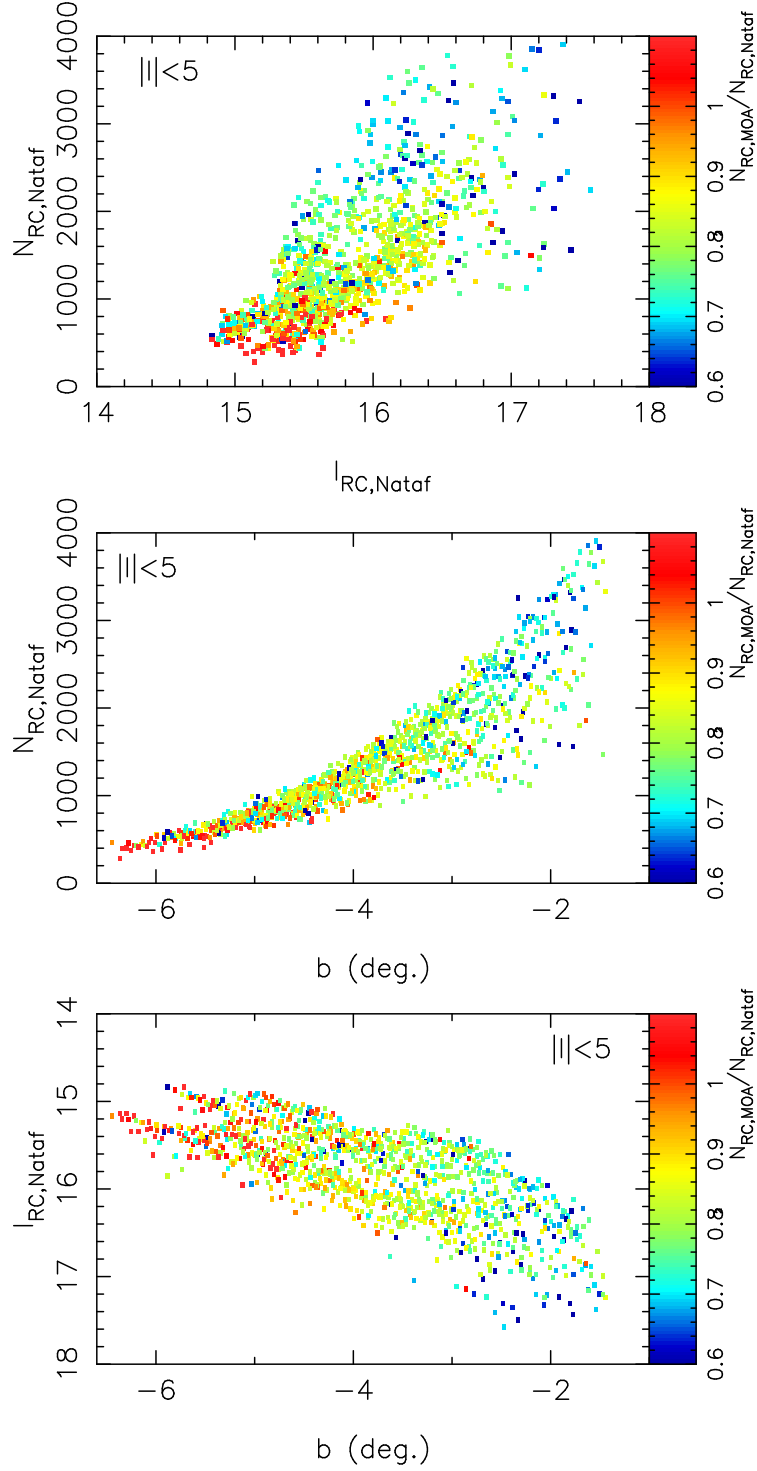


Fig. 3.—: The number of RCG measured by MOA over that measured by OGLE,  $f_{\text{RC}} = N_{\text{RC,MOA}}/N_{\text{RC,Nataf}}$  (color-coded) of subfields with  $|l| \leq 5^\circ$  in  $(I_{\text{RC,Nataf}}, N_{\text{RC,Nataf}})$  (top panel),  $(b, N_{\text{RC,Nataf}})$  (middle panel) and  $(b, I_{\text{RC,Nataf}})$  (bottom panel) planes.

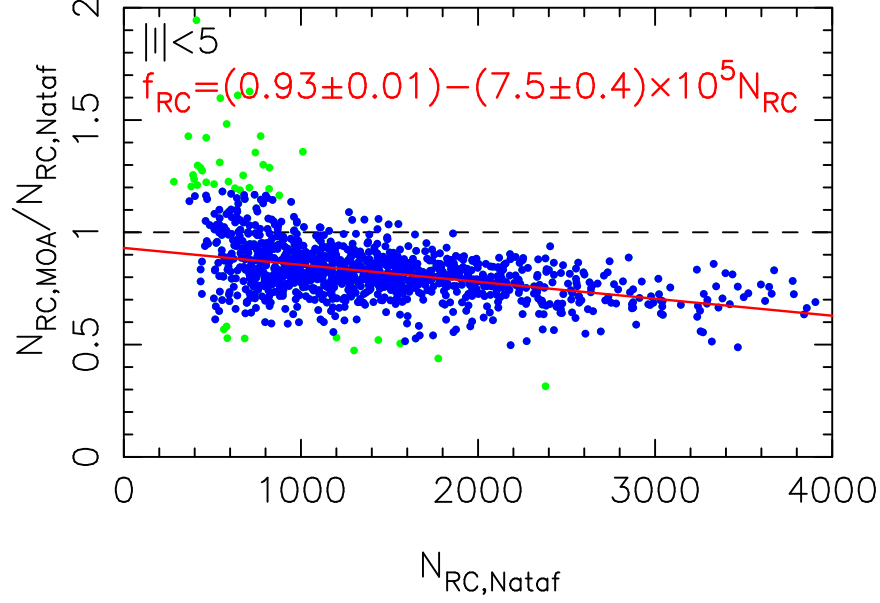


Fig. 4.—: The number of RCG measured by MOA over that measured by OGLE,  $f_{\text{RC}} = N_{\text{RC,MOA}}/N_{\text{RC,Nataf}}$  for subfields with  $|l| \leq 5^\circ$  as a function of  $N_{\text{RC,Nataf}}$ . The red line indicates the best fit to the blue dots where  $3\sigma$  outliers (green dots) are recursively rejected.

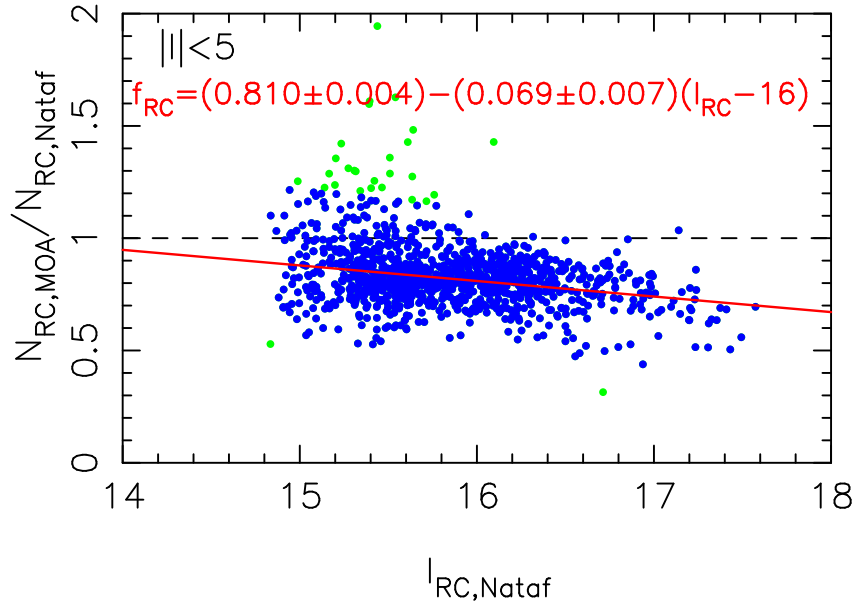


Fig. 5.—: The number of RCG by MOA over that by OGLE,  $f_{\text{RC}} = N_{\text{RC,MOA}}/N_{\text{RC,Nataf}}$  of subfields with  $|l| \leq 5^\circ$  as a function of  $I_{\text{RC,Nataf}}$ . The red lines indicate the best fit by using the blue dots where  $3\sigma$  outliers (green dots) are recursively rejected.

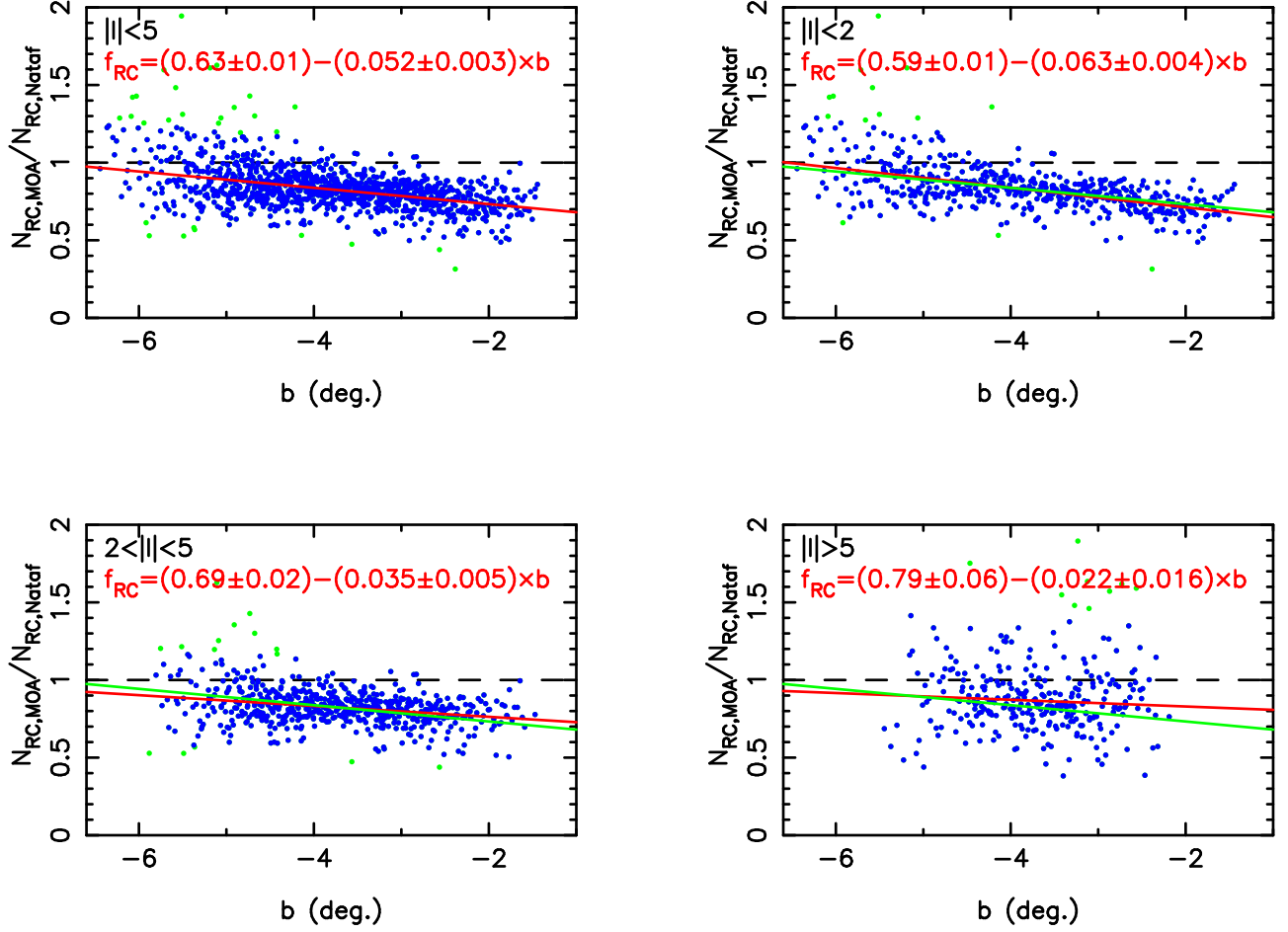


Fig. 6.—: The number counts of RCG by MOA over that by OGLE,  $f_{\text{RC}} = N_{\text{RC,MOA}} / N_{\text{RC,Nataf}}$  for the subfields. The top-left, top-right, bottom-left and bottom-right panels are for subfields with the galactic longitude of  $|l| \leq 5^\circ$ ,  $|l| \leq 2^\circ$ ,  $2^\circ < |l| \leq 5^\circ$  and  $|l| > 5^\circ$ , respectively. The red lines indicate the best fit using the blue dots, where  $3\sigma$  outliers (green dots) are recursively rejected. The green lines indicate the best fit for  $|l| \leq 5^\circ$  as a comparison. They are all consistent with each other.

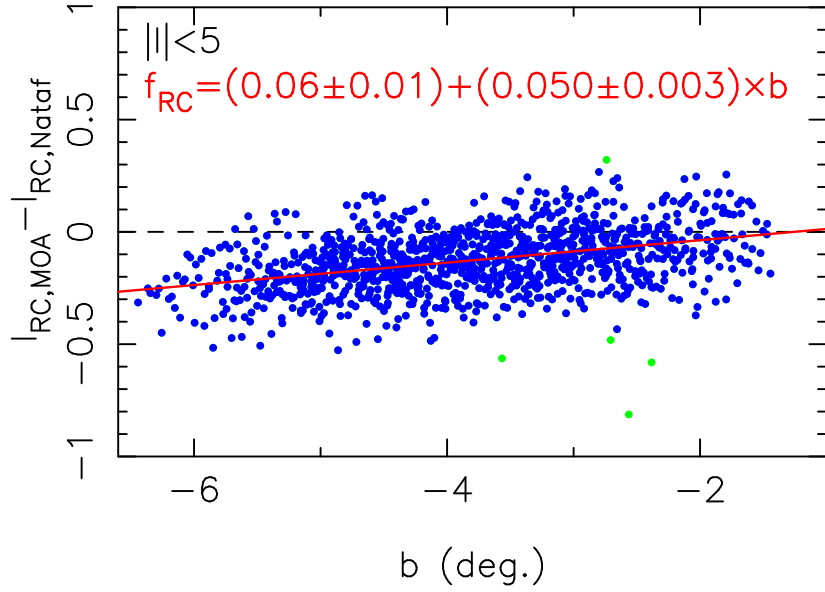


Fig. 7.—: The difference between  $I_{\text{RC}}$  by MOA and that by OGLE,  $I_{\text{RC,MOA}} - I_{\text{RC,Nataf}}$  of subfields with the galactic longitude of  $|l| \leq 5^\circ$ . The red line indicates the best fit by using the blue dots where  $3\sigma$  outliers (green dots) are recursively rejected.

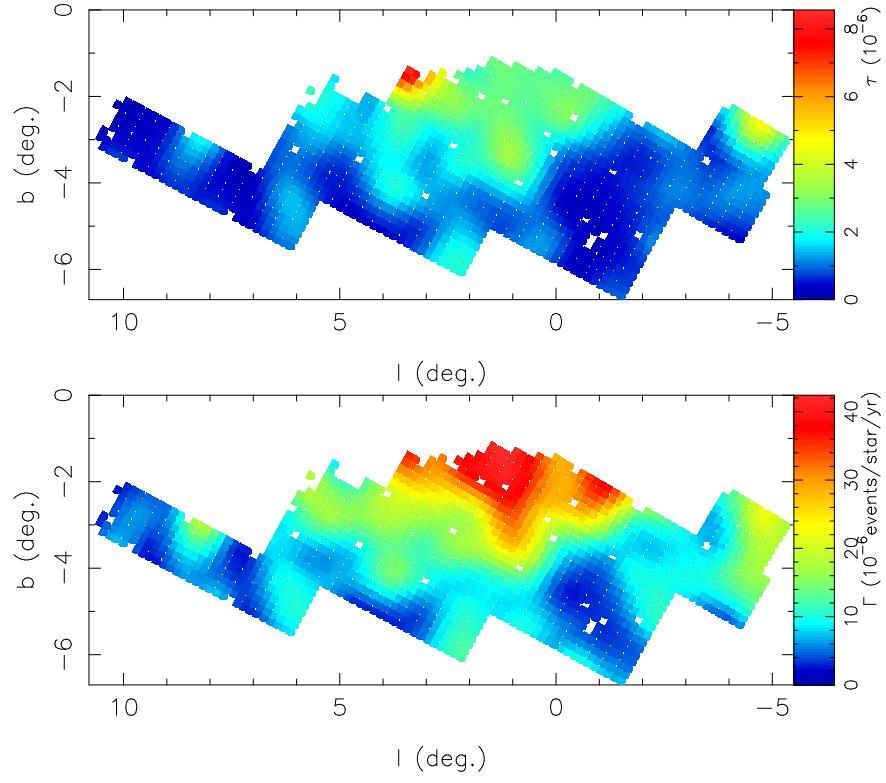


Fig. 8.—: False color maps of the measured optical depth,  $\tau_{200}$  (top panel) and the event rate per star per year,  $\Gamma$  (bottom panel).

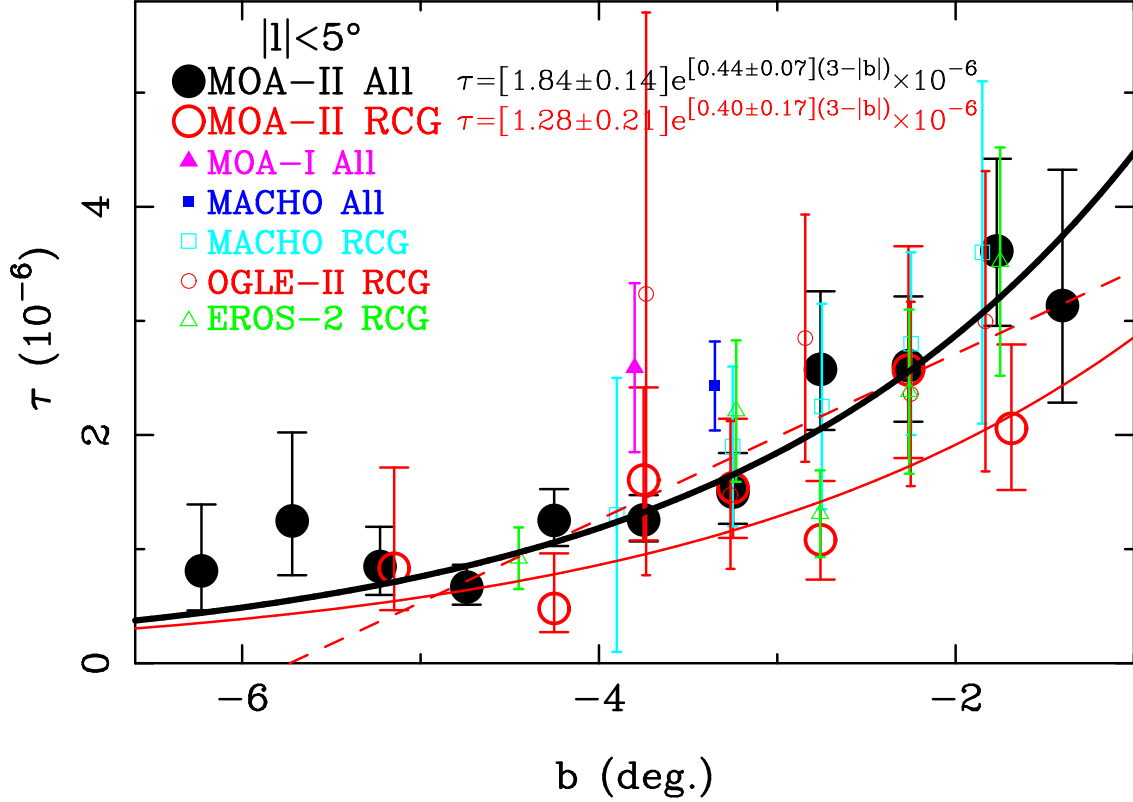


Fig. 9.—: The measured optical depth for the all-source (black filled circle) and RCG (red large open circle) samples as a function of galactic latitude  $b$  for  $|l| < 5^\circ$ . The subfields are combined into bins of width  $\Delta b = 0.5^\circ$ . The binned values are listed in Table 2 and 3. The filled circles, triangles and squares indicate  $\tau$  for all-source samples measured by MOA-II (this work), MOA-I and MACHO surveys, respectively. The red circles, open squares, circles and triangles denote the  $\tau$  for RCG samples by the MOA-II (this work), MACHO, OGLE-II and EROS surveys, respectively. The thick black and thin red solid lines indicate the best fit exponential functions for the MOA-II measurements. The red dashed line denotes the best linear model for the OGLE-II RCG sample as a comparison.



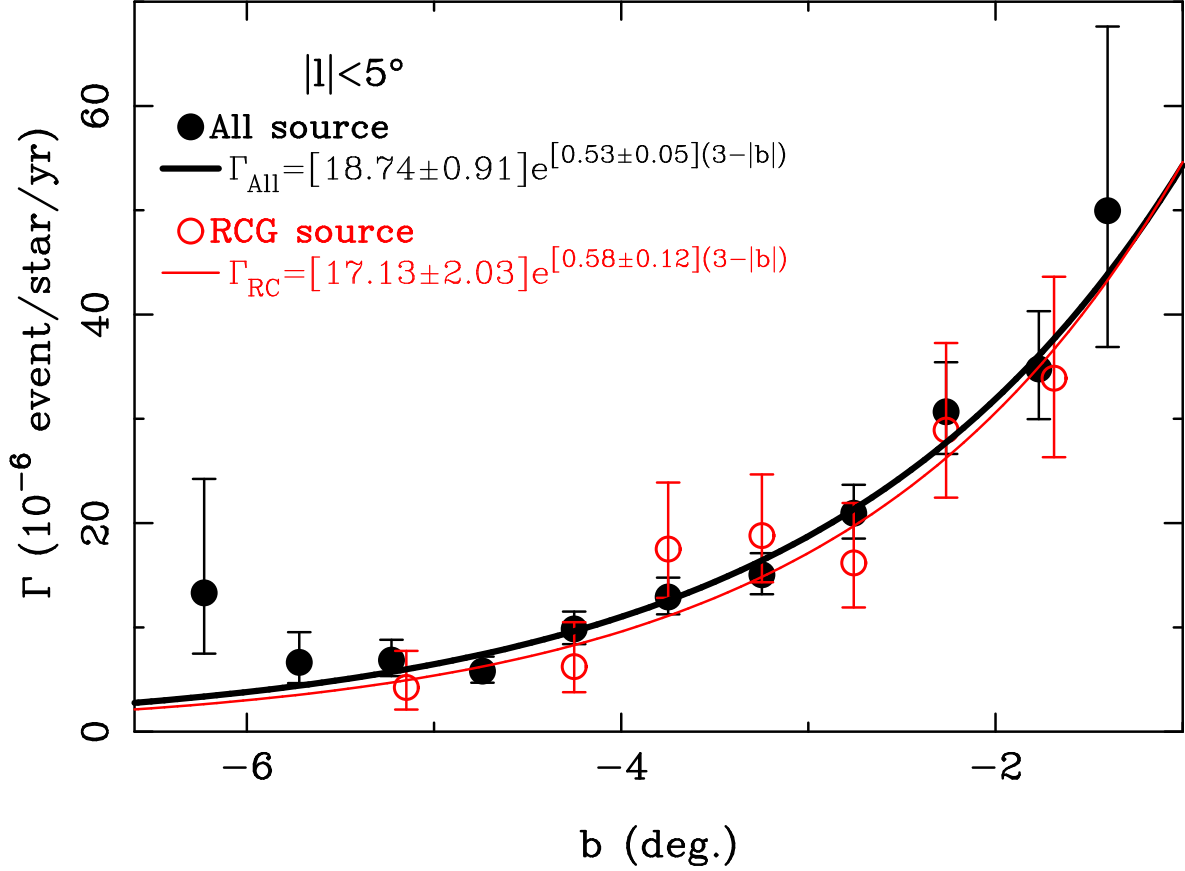


Fig. 10.—: The event rate per star per year,  $\Gamma$ , for the all-source (black filled circle) and RCG (red open circle) samples as a function of the galactic latitude  $b$  for  $|l| < 5^\circ$ . The subfields are combined into bins of width  $\Delta b = 0.5^\circ$  for display purposes only, as the fitting was done using the unbinned subfield data with the Poisson statistics fitting method. The plotted values are listed in Tables 2 and 3. The thick black and thin red solid lines indicate the best fit exponential functions for the all-source and RCG samples, respectively.

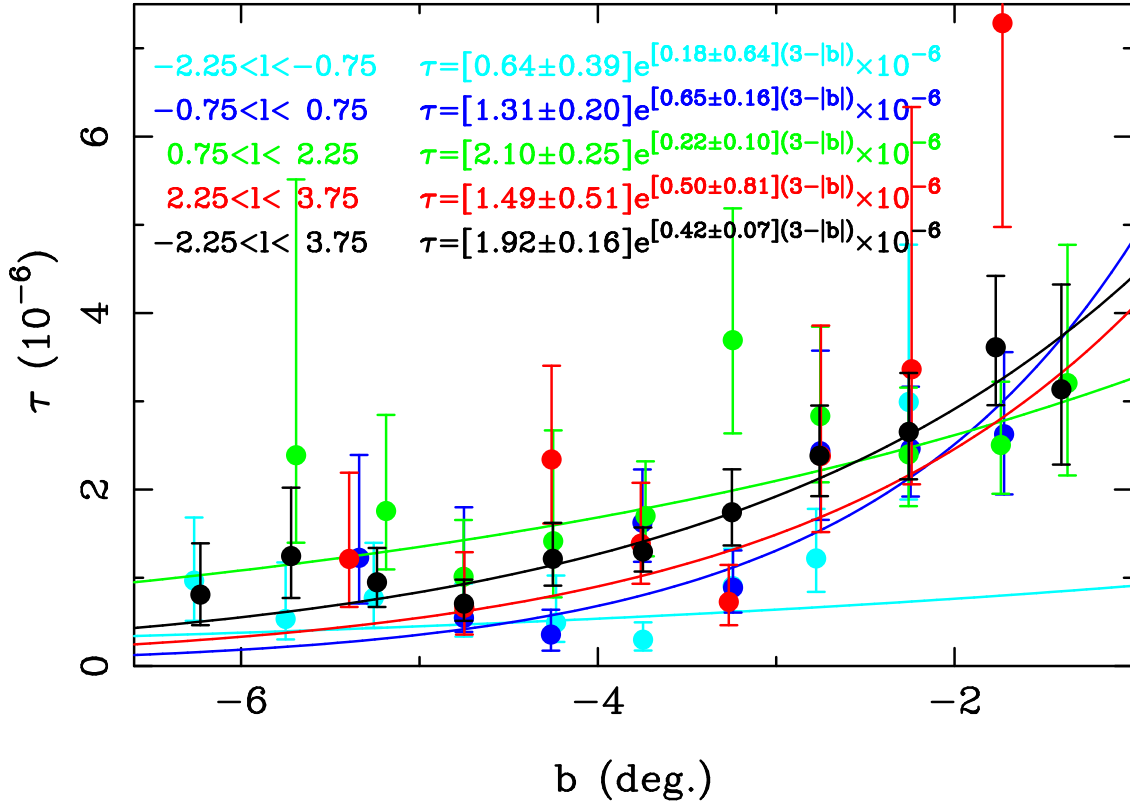


Fig. 11.—: The optical depth for events with  $t_E < 200$  days,  $\tau_{200}$ , for the all-source sample as a function of the galactic latitude  $b$  for different bins in Galactic longitude,  $l$ . The curves show the best exponential fit in  $b$ . The black curve is the fit to all the events with  $-2^\circ.25 < l < 3^\circ.75$ .

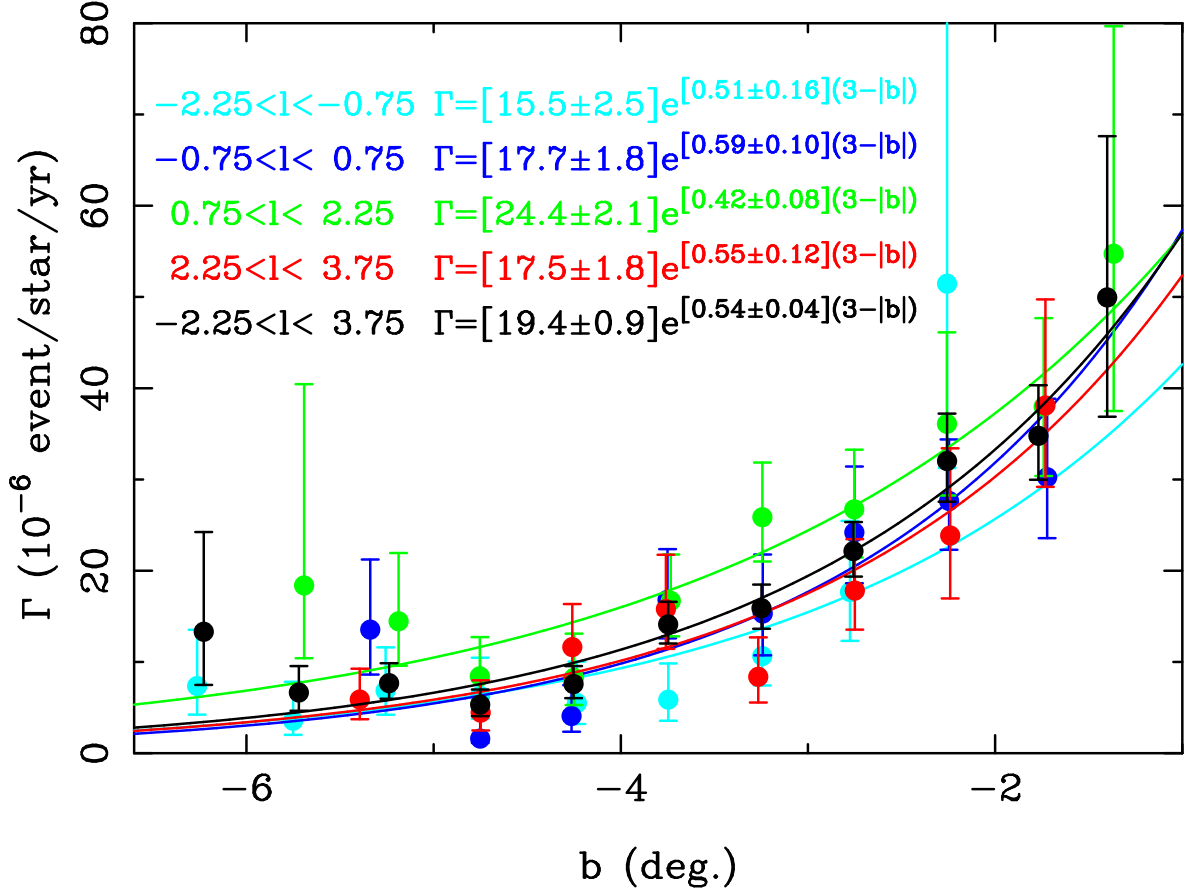


Fig. 12.—: The event rate per star per year,  $\Gamma$ , for the all-source sample as a function of the galactic latitude  $b$  for different bins in Galactic longitude,  $l$ . The curves show the best exponential fit in  $b$  to the unbinned subfield data. The black curve is the fit to all the events with  $-2^{\circ}.25 < l < 3^{\circ}.75$ , and it provides a reasonable fit to all the longitude bins, except the  $0^{\circ}.75 < l < 2^{\circ}.25$  bin, where there is an enhancement to the rate.

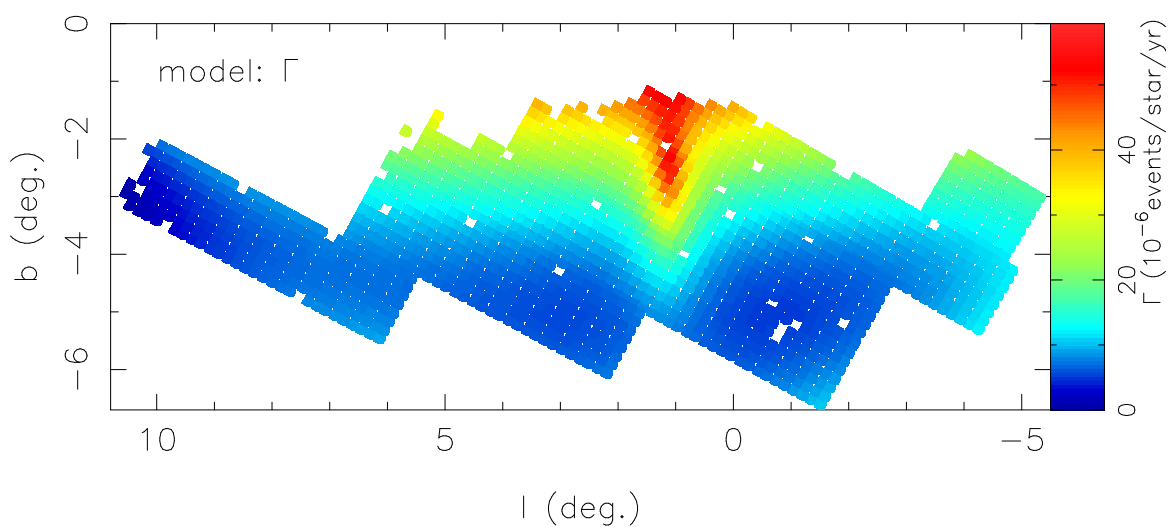


Fig. 13.—: A 16-parameter model of microlensing event rate per star for the all-source sample. The model is described by Equation (6) with parameters given in Table 5.

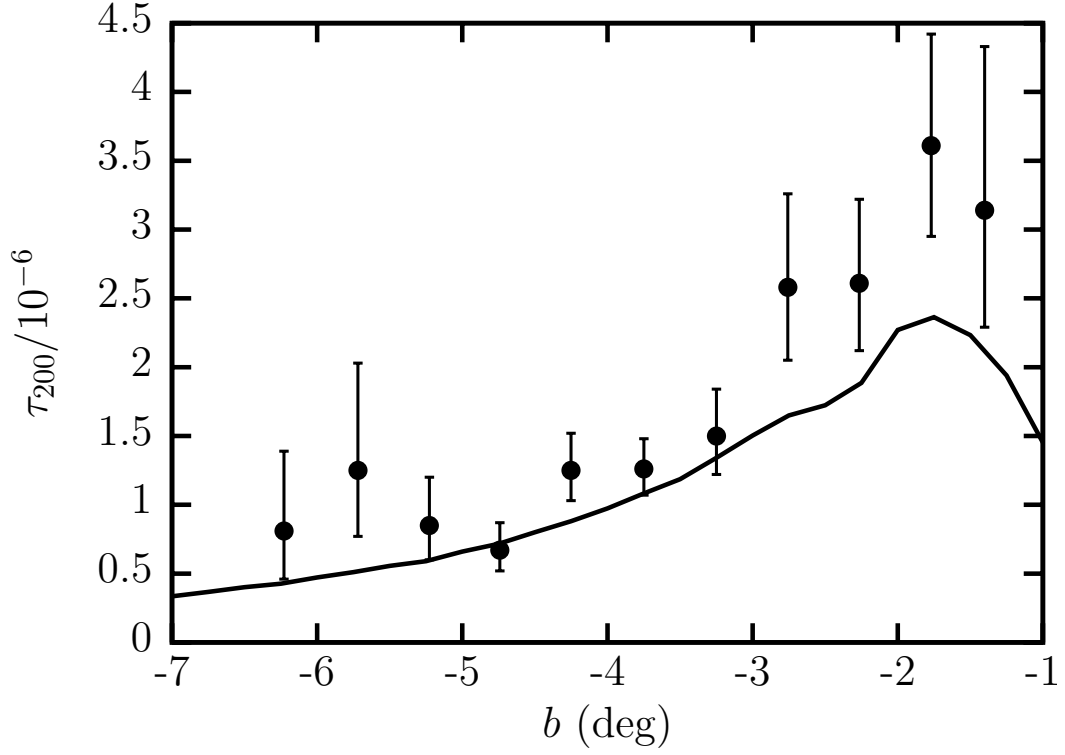


Fig. 14.—: The optical depth for events with  $t_E < 200$  days,  $\tau_{200}$ , for the all-source sample as a function of the galactic latitude  $b$  (filled circles with error bars), and the theoretical model from the Besançon model by Awiphan, Kerins & Robin (2016) (solid line). It is better agreement than the original  $\tau$  measurements by Sumi et al. (2013), while they are still slightly higher.

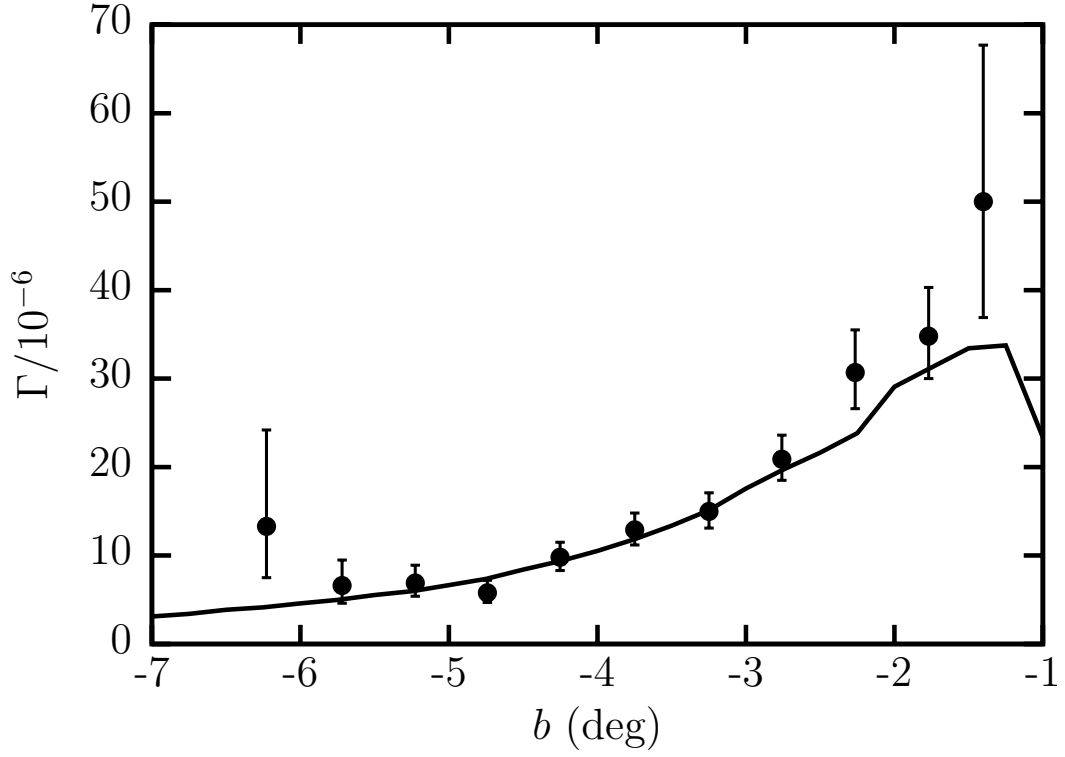


Fig. 15.—: The event rate per star per year,  $\Gamma$ , for the all-source sample as a function of the galactic latitude  $b$  (filled circles with error bars), and the theoretical model from the Besançon model by Awiphan, Kerins & Robin (2016) (solid line). They are consistent.

Table 1. MOA-II Galactic bulge fields with Galactic coordinates of the mean field center ( $\langle l \rangle$ ,  $\langle b \rangle$ ), the number of subfields used ( $N_{\text{sub}}$ ), the number of frames ( $N_f$ ), the number of source stars ( $N_s$  in thousands), the number of microlensing events ( $N_{\text{ev}}$ ), the microlensing event rate per star per year ( $\Gamma$ ), the microlensing event rate per square degree per year ( $\Gamma_{\text{deg}^2}$ ), the optical depth ( $\tau_{200}$ ), and the mean detection efficiency weighted  $t_E$ .

Field	$\langle l \rangle$ ( $^\circ$ )	$\langle b \rangle$ ( $^\circ$ )	$N_{\text{sub}}$	$N_f$	$N_s$ ( $10^3$ )	$N_{\text{ev}}$	$\tau_{200}$ ( $10^{-6}$ )	$\Gamma(10^{-6})$ ( $\text{star}^{-1}\text{yr}^{-1}$ )	$\Gamma_{\text{deg}^2}$ ( $\text{deg.}^{-2}\text{yr}^{-1}$ )	$\langle t_E \rangle$ (day)
gb1	-4.3306	-3.1119	79	2253	5356	22	$2.03^{+1.53}_{-0.69}$	$15.0^{+4.2}_{-3.3}$	$37.0^{+10.4}_{-8.1}$	30.6
gb2	-3.8624	-4.3936	79	2386	5527	17	$0.80^{+0.25}_{-0.19}$	$9.7^{+2.7}_{-2.1}$	$24.7^{+6.9}_{-5.4}$	18.8
gb3	-2.3463	-3.5133	79	2067	5635	19	$1.07^{+0.34}_{-0.26}$	$9.1^{+2.4}_{-1.9}$	$23.5^{+6.2}_{-4.8}$	26.7
gb4	-0.8210	-2.6317	77	2985	5506	41	$2.31^{+0.58}_{-0.46}$	$27.0^{+5.6}_{-4.6}$	$70.2^{+14.7}_{-11.9}$	19.4
gb5	0.6544	-1.8595	65	8229	6106	67	$2.81^{+0.45}_{-0.39}$	$36.6^{+4.9}_{-4.4}$	$124.9^{+16.7}_{-15.1}$	17.4
gb6	1.8405	-1.4890	11	1779	446	4	$1.38^{+0.90}_{-0.57}$	$18.5^{+12.3}_{-7.4}$	$27.3^{+18.2}_{-10.9}$	16.9
gb7	-1.7147	-4.5992	78	1970	5082	15	$0.70^{+0.25}_{-0.18}$	$8.4^{+2.6}_{-2.0}$	$20.0^{+6.1}_{-4.6}$	18.8
gb8	-0.1937	-3.7495	78	2139	6366	16	$0.71^{+0.22}_{-0.17}$	$7.4^{+2.1}_{-1.7}$	$22.1^{+6.3}_{-4.9}$	21.7
gb9	1.3329	-2.8786	79	8301	9881	74	$2.59^{+0.47}_{-0.39}$	$26.5^{+3.5}_{-3.1}$	$120.4^{+15.9}_{-14.0}$	22.2
gb10	2.8448	-2.0903	70	1992	4978	36	$3.60^{+1.23}_{-0.92}$	$28.9^{+6.4}_{-5.1}$	$74.6^{+16.6}_{-13.3}$	28.3
gb11	-1.1093	-5.7257	76	2004	4023	8	$0.44^{+0.21}_{-0.14}$	$5.9^{+3.0}_{-2.0}$	$11.3^{+5.7}_{-3.8}$	16.9
gb12	0.4391	-4.8658	79	1790	5510	12	$0.94^{+0.43}_{-0.30}$	$6.4^{+2.1}_{-1.6}$	$16.2^{+5.4}_{-4.1}$	33.2
gb13	1.9751	-4.0190	79	1811	8133	27	$1.76^{+0.64}_{-0.48}$	$13.5^{+3.1}_{-2.5}$	$50.7^{+11.5}_{-9.3}$	29.6
gb14	3.5083	-3.1698	79	1770	7934	29	$1.58^{+0.57}_{-0.42}$	$14.0^{+2.9}_{-2.4}$	$51.2^{+10.8}_{-8.8}$	25.5
gb15	4.9940	-2.4496	62	1952	2448	14	$1.77^{+0.64}_{-0.47}$	$17.1^{+5.3}_{-4.1}$	$24.6^{+7.6}_{-5.8}$	23.5
gb16	2.6048	-5.1681	79	1756	5627	17	$1.40^{+0.50}_{-0.38}$	$9.0^{+2.5}_{-2.0}$	$23.3^{+6.5}_{-5.1}$	35.3
gb17	4.1498	-4.3365	79	1792	6448	16	$1.14^{+0.41}_{-0.30}$	$8.2^{+2.4}_{-1.9}$	$24.3^{+7.1}_{-5.5}$	31.7
gb18	5.6867	-3.5055	78	1799	4722	13	$0.82^{+0.33}_{-0.24}$	$7.8^{+2.6}_{-2.0}$	$17.1^{+5.6}_{-4.3}$	23.9
gb19	6.5534	-4.5749	78	1704	4424	12	$0.94^{+0.36}_{-0.26}$	$7.1^{+2.4}_{-1.8}$	$14.6^{+4.9}_{-3.7}$	30.0
gb20	8.1025	-3.7531	79	1679	3673	12	$0.97^{+0.37}_{-0.27}$	$8.9^{+3.0}_{-2.2}$	$15.1^{+5.0}_{-3.8}$	24.6
gb21	9.6172	-2.9318	73	1659	2419	3	$0.26^{+0.23}_{-0.11}$	$3.5^{+2.6}_{-1.7}$	$4.2^{+3.1}_{-2.0}$	17.0
all	1.8530	-3.6890	1536	—	110253	474	$1.53^{+0.12}_{-0.11}$	$14.5^{+0.7}_{-0.7}$	$37.8^{+1.9}_{-1.9}$	24.0
all <sub>RC</sub> *	1.8530	-3.6890	1536	—	7997	83	$1.28^{+0.22}_{-0.19}$	$15.1^{+1.8}_{-1.6}$	$2.9^{+0.3}_{-0.3}$	19.2

Note. — The values are for the all-source sample except for all<sub>RC</sub> which is for the RCG source sample.



Table 2. Microlensing optical depth and event rates binned in  $b$  for the all-source sample with  $|l| < 5^\circ$ .

$\langle b \rangle^*$ ( $^\circ$ )	$N_{\text{sub}}$	$N_s$	$N_{\text{ev}}$	$\tau(10^{-6})$	$\Gamma(10^{-6})$ ( $\text{star}^{-1} \text{ yr}^{-1}$ )	$\Gamma_{\text{deg}^2}$ ( $\text{deg.}^{-2} \text{ yr}^{-1}$ )
-1.4012	20	687319	12	$3.14^{+1.19}_{-0.85}$	$50.0^{+17.7}_{-13.1}$	$62.4^{+22.1}_{-16.3}$
-1.7690	70	5032788	52	$3.61^{+0.81}_{-0.66}$	$34.8^{+5.5}_{-4.8}$	$90.9^{+14.5}_{-12.6}$
-2.2645	114	9056629	70	$2.61^{+0.61}_{-0.49}$	$30.7^{+4.8}_{-4.1}$	$88.6^{+13.7}_{-11.7}$
-2.7576	146	13187560	75	$2.58^{+0.68}_{-0.53}$	$20.9^{+2.7}_{-2.4}$	$68.8^{+9.0}_{-7.9}$
-3.2486	168	15542979	67	$1.50^{+0.34}_{-0.28}$	$15.0^{+2.1}_{-1.9}$	$50.6^{+7.0}_{-6.3}$
-3.7490	172	14776708	58	$1.26^{+0.22}_{-0.19}$	$12.9^{+1.9}_{-1.7}$	$40.3^{+5.8}_{-5.2}$
-4.2512	172	13727488	43	$1.25^{+0.27}_{-0.22}$	$9.8^{+1.7}_{-1.5}$	$28.6^{+4.9}_{-4.2}$
-4.7410	154	10977355	22	$0.67^{+0.20}_{-0.15}$	$5.8^{+1.4}_{-1.1}$	$15.0^{+3.6}_{-2.9}$
-5.2270	101	6558015	16	$0.85^{+0.35}_{-0.25}$	$6.9^{+2.0}_{-1.5}$	$16.2^{+4.6}_{-3.6}$
-5.7197	56	3099616	8	$1.25^{+0.78}_{-0.48}$	$6.6^{+2.9}_{-2.0}$	$13.4^{+5.8}_{-4.0}$
-6.2282	21	1030160	4	$0.81^{+0.58}_{-0.35}$	$13.3^{+10.9}_{-5.8}$	$23.7^{+19.5}_{-10.4}$

Note. — \*Average galactic latitude of fields in each bin.  $N_{\text{sub}}$ ,  $N_s$  and  $N_{\text{ev}}$  indicate the number of subfields, source stars and microlensing events in each bin.

Table 3. Microlensing optical depth and event rates binned in  $b$  for the RCG sample with  $|l| < 5^\circ$ .

$\langle b \rangle^*$ ( $^\circ$ )	$N_{\text{sub}}$	$N_s$	$N_{\text{ev}}$	$\tau(10^{-6})$	$\Gamma(10^{-6})$ ( $\text{star}^{-1} \text{ yr}^{-1}$ )	$\Gamma_{\text{deg}^2}$ ( $\text{deg.}^{-2} \text{ yr}^{-1}$ )
-1.6872	90	715368	16	$2.06^{+0.74}_{-0.54}$	$33.9^{+9.7}_{-7.6}$	$9.8^{+2.8}_{-2.2}$
-2.2645	114	807674	16	$2.57^{+1.08}_{-0.77}$	$28.9^{+8.3}_{-6.5}$	$7.5^{+2.2}_{-1.7}$
-2.7576	146	976651	11	$1.08^{+0.52}_{-0.35}$	$16.2^{+5.7}_{-4.3}$	$3.9^{+1.4}_{-1.0}$
-3.2486	168	1051602	14	$1.54^{+0.60}_{-0.44}$	$18.8^{+5.9}_{-4.5}$	$4.3^{+1.3}_{-1.0}$
-3.7490	172	952935	11	$1.61^{+0.81}_{-0.53}$	$17.5^{+6.4}_{-4.7}$	$3.5^{+1.3}_{-0.9}$
-4.2512	172	863385	4	$0.48^{+0.48}_{-0.21}$	$6.2^{+4.3}_{-2.4}$	$1.1^{+0.8}_{-0.4}$
-5.1480	332	1368724	3	$0.83^{+0.88}_{-0.37}$	$4.2^{+3.5}_{-2.1}$	$0.6^{+0.5}_{-0.3}$

Note. — \*Average galactic latitude of fields in each bin. The notation is the same as in Table 2.

Table 4. Average microlensing optical depth and event rates at the position of each subfield for the all-source sample.

subfield	$l$ ( $^{\circ}$ )	$b$ ( $^{\circ}$ )	$N_{\text{sub}}$	$N_s$	$N_{\text{ev}}$	$\tau(10^{-6})$	$\Gamma(10^{-6})$ ( $\text{star}^{-1}\text{yr}^{-1}$ )	$\Gamma_{\text{deg}^2}$ ( $\text{deg.}^{-2}\text{yr}^{-1}$ )
gb5-1-3	1.1704	-1.3459	58	4796785	55	$2.9^{+0.7}_{-0.5}$	$42.4^{+12.9}_{-10.2}$	$109.0^{+33.1}_{-26.3}$
gb5-1-7	1.3125	-1.2630	51	3917583	46	$2.9^{+0.7}_{-0.6}$	$42.4^{+15.3}_{-10.9}$	$96.6^{+34.9}_{-24.8}$
gb5-2-2	0.7835	-1.3776	59	5177353	59	$2.7^{+0.5}_{-0.5}$	$40.2^{+11.7}_{-9.1}$	$118.0^{+34.5}_{-26.7}$
gb5-2-3	0.8685	-1.5224	69	6310401	67	$2.7^{+0.5}_{-0.4}$	$40.2^{+9.9}_{-7.9}$	$126.1^{+31.1}_{-24.8}$
gb5-2-6	0.9280	-1.2935	54	4439824	49	$2.8^{+0.6}_{-0.5}$	$41.7^{+13.4}_{-10.1}$	$112.9^{+36.1}_{-27.4}$
gb5-2-7	1.0130	-1.4379	63	5557000	63	$2.8^{+0.6}_{-0.5}$	$41.7^{+11.2}_{-8.7}$	$120.2^{+32.1}_{-25.2}$
gb5-3-1	0.3942	-1.4104	53	5008885	52	$2.7^{+0.6}_{-0.5}$	$34.2^{+11.4}_{-8.7}$	$103.0^{+34.2}_{-26.1}$
gb5-3-2	0.4788	-1.5549	67	6338841	63	$2.7^{+0.6}_{-0.5}$	$35.1^{+9.3}_{-7.3}$	$114.3^{+30.2}_{-23.7}$
gb5-3-3	0.5639	-1.6998	78	7640959	74	$2.7^{+0.5}_{-0.4}$	$35.9^{+8.3}_{-6.9}$	$126.2^{+29.1}_{-24.1}$
gb5-3-6	0.6239	-1.4697	65	5938827	65	$2.7^{+0.5}_{-0.4}$	$37.8^{+10.5}_{-8.1}$	$117.9^{+32.8}_{-25.4}$
gb5-3-7	0.7091	-1.6146	76	7142733	75	$2.7^{+0.5}_{-0.4}$	$38.4^{+9.0}_{-7.2}$	$128.6^{+30.2}_{-24.0}$
gb5-4-0	0.0089	-1.4439	48	4203315	37	$2.5^{+0.7}_{-0.6}$	$28.8^{+11.3}_{-8.5}$	$82.1^{+32.2}_{-24.2}$
gb5-4-1	0.0918	-1.5877	59	5398262	52	$2.7^{+0.7}_{-0.5}$	$29.6^{+9.4}_{-7.0}$	$92.6^{+29.2}_{-21.9}$
gb5-4-2	0.1755	-1.7322	73	6845398	65	$2.8^{+0.6}_{-0.5}$	$30.5^{+7.9}_{-6.5}$	$104.0^{+27.0}_{-22.1}$
gb5-4-3	0.2599	-1.8771	81	7762864	70	$2.8^{+0.6}_{-0.5}$	$31.3^{+7.2}_{-5.9}$	$114.7^{+26.5}_{-21.5}$
gb5-4-5	0.2356	-1.5028	56	5313798	53	$2.7^{+0.7}_{-0.5}$	$31.6^{+10.1}_{-7.8}$	$97.5^{+31.1}_{-24.2}$
gb5-4-6	0.3197	-1.6474	70	6687816	67	$2.7^{+0.6}_{-0.5}$	$32.7^{+8.6}_{-6.8}$	$110.1^{+28.9}_{-22.8}$
gb5-4-7	0.4044	-1.7925	81	7829673	76	$2.8^{+0.5}_{-0.5}$	$33.7^{+7.9}_{-6.6}$	$121.9^{+28.4}_{-23.9}$
gb5-5-0	-0.2872	-1.6227	53	4406168	43	$2.6^{+0.7}_{-0.5}$	$29.2^{+12.7}_{-8.9}$	$81.0^{+35.3}_{-24.8}$
gb5-5-1	-0.2055	-1.7661	63	5424411	50	$2.8^{+0.7}_{-0.6}$	$28.7^{+10.1}_{-7.6}$	$86.8^{+30.6}_{-22.9}$
gb5-5-2	-0.1227	-1.9100	76	6720615	57	$2.9^{+0.7}_{-0.6}$	$28.5^{+9.0}_{-6.8}$	$93.1^{+29.5}_{-22.4}$

Note. — The averages include all the subfields within  $1^{\circ}$  of the center of each subfield with a Gaussian weighting function with  $\sigma = 0^{\circ}.4$ .  $N_{\text{sub}}$ ,  $N_s$  and  $N_{\text{ev}}$  are numbers of subfields, source stars and microlensing events in this  $1^{\circ}$  circle, respectively. A complete electronic version of this table is available at <http://iral2.ess.sci.osaka-u.ac.jp/~sumi/OPTMOAILNataf/Table4.dat>

Table 5. The best 2D model parameters for  $\Gamma$ .

param	value
$a_0$	76.558396
$a_1$	0.758556
$a_2$	32.598859
$a_3$	-0.274198
$a_4$	0.178113
$a_5$	4.408679
$a_6$	-0.017363
$a_7$	-0.104587
$a_8$	-0.006764
$a_9$	0.157305
$a_{10}$	0.651233
$a_{11}$	-0.717574
$a_{12}$	0.163776
$a_{13}$	0.324459
$a_{14}$	0.005950
$a_{15}$	0.032564

Note. — The model parameters are defined in Equation (6).